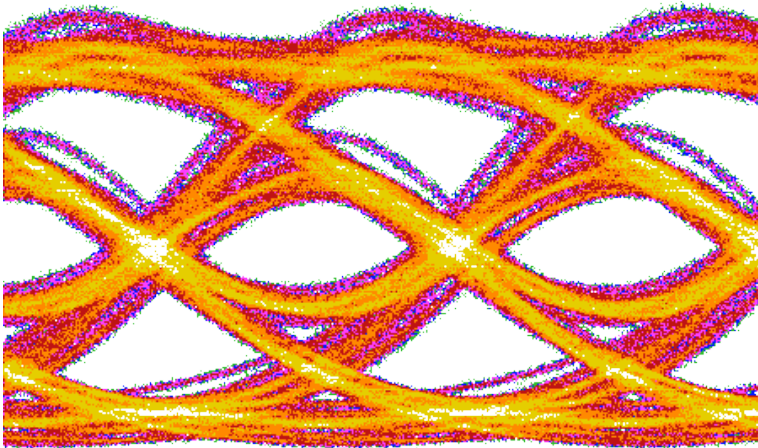


# CHALMERS



## Influence of Damping on High-Speed VCSEL Data Transmission

*Master's thesis in Photonics*

EMANUEL HAGLUND

Photonics Laboratory  
Department of Microtechnology and Nanoscience – MC2  
CHALMERS UNIVERSITY OF TECHNOLOGY  
Göteborg, Sweden 2013



MASTER'S THESIS IN PHOTONICS

Influence of Damping on High-Speed VCSEL  
Data Transmission

EMANUEL HAGLUND



Photonics Laboratory

Department of Microtechnology and Nanoscience – MC2

CHALMERS UNIVERSITY OF TECHNOLOGY

Göteborg, Sweden 2013

# Influence of Damping on High-Speed VCSEL Data Transmission

EMANUEL HAGLUND

Contact: haglund.emanuel@gmail.com

© Emanuel Haglund, 2013

Photonics Laboratory  
Department of Microtechnology and Nanoscience – MC2  
Chalmers University of Technology  
SE-412 96 Göteborg  
Sweden  
Telephone: +46 (0)31-772 1000

Cover:

Left: Eye diagram of a 50 Gbit/s signal transmitted over 50 m of multimode fiber.

Right: Microscope image of a fully processed high-speed VCSEL on wafer.

Printed by Chalmers Reproservice  
Göteborg, Sweden 2013

Influence of Damping on High-Speed VCSEL Data Transmission  
Master's thesis in Photonics  
EMANUEL HAGLUND  
Photonics Laboratory  
Department of Microtechnology and Nanoscience – MC2  
Chalmers University of Technology

## Abstract

The vertical-cavity surface-emitting laser (VCSEL) is a low-cost light source with properties well suited for short-reach high-speed data transmission. Due to the increasing demand for high-speed data communication capacity, both in data centers and home connections, there is need for low-cost solutions operating at high bit rates, which makes the VCSEL an attractive option in such optical systems. Commercially available VCSELs are, however, limited to bit rates of around 10 Gbit/s, which is far lower than the data rates specified in upcoming standards. This means that the development of higher speed VCSELs is required.

This work has studied the influence of damping on high-speed VCSEL data transmission performance, through an investigation of the large signal properties. VCSELs with different damping (obtained by shallow surface etches of different depths) were characterized through static and dynamic measurements, with emphasis on characterizations during large signal data transmission.

Through investigations of the timing jitter and the bit error rate (BER), it was found that using a VCSEL with a  $K$ -factor of 0.16 ns and a  $D$ -factor of  $9 \text{ GHz}/\sqrt{\text{mA}}$ , provided the best high-speed properties among the tested devices. This particular VCSEL was able to achieve record high data rates, with 57 Gbit/s back-to-back (BTB), and 55 Gbit/s and 43 Gbit/s over 50 m and 100 m of OM4-fiber, respectively.

Keywords: Vertical-cavity surface-emitting laser (VCSEL), damping, photon lifetime, laser dynamics, high-speed modulation, data transmission, timing jitter, dual-Dirac model



# Acknowledgements

First of all, I would like to thank Professor Anders Larsson for allowing me to work in this exciting project. I am most grateful to my supervisors Erik Haglund and Petter Westbergh for their excellent support and guidance throughout this Master's project. Furthermore, I would like to thank Rashid Safaisini and Krzysztof Szczerba for their valuable assistance in the lab. I would also like to thank all the people of the Photonics Laboratory, both for the warm welcoming and for sharing the measurement equipment. Finally, I would like to express my deepest gratitude to my beloved Linda for her endless support and for always believing in me.

Emanuel Haglund

*Göteborg  
June 2013*



# Nomenclature

BER	Bit Error Rate	VCSEL	Vertical-Cavity Surface-Emitting Laser
BERT	Bit Error Rate Tester	VOA	Variable Optical Attenuator
BPG	Bit Pattern Generator		
BTB	Back-To-Back		
BUJ	Bounded Uncorrelated Jitter		
CDF	Cumulative Density Function		
DBR	Distributed Bragg Reflector		
DCD	Duty Cycle Distortion		
DDJ	Data Dependent Jitter		
DJ	Deterministic Jitter		
EA	Error Analyzer		
HPC	High-Performance Computing		
ISI	Inter Symbol Interference		
MMF	Multimode Fiber		
NRZ	Non Return to Zero		
OOK	On-Off Keying		
PDF	Probability Density Function		
pp	peak-to-peak		
PRBS	Pseudo Random Bit Sequence		
RJ	Random Jitter		
RMS	Root-Mean-Square		
SNR	Signal-to-Noise-Ratio		
TJ	Total Jitter		
UI	Unit Interval		



# Contents

<b>Abstract</b>	<b>i</b>
<b>Acknowledgements</b>	<b>iii</b>
<b>Nomenclature</b>	<b>v</b>
<b>1 Introduction</b>	<b>1</b>
1.1 Purpose and Objective . . . . .	2
1.2 Scope . . . . .	2
<b>2 Static Operation of VCSELs</b>	<b>3</b>
2.1 Semiconductor Laser . . . . .	3
2.2 Vertical-Cavity Surface-Emitting Laser . . . . .	4
<b>3 Dynamic Operation of VCSELs</b>	<b>7</b>
3.1 Rate Equations . . . . .	7
3.2 Small Signal Analysis . . . . .	8
3.2.1 Damping . . . . .	9
3.2.2 Bandwidth . . . . .	10
3.2.3 $D$ -Factor . . . . .	10
3.2.4 Electrical Parasitics . . . . .	10
3.3 Tuning the VCSEL Damping . . . . .	11
<b>4 Data Transmission</b>	<b>13</b>
4.1 Bit Error Rate . . . . .	13
4.2 Eye Diagram . . . . .	14
4.3 Timing Jitter . . . . .	14
4.3.1 Random Jitter . . . . .	15
4.3.2 Deterministic Jitter . . . . .	15
4.3.3 Total Jitter . . . . .	16
4.4 The Dual-Dirac Model . . . . .	17
4.4.1 Limitations of the Dual-Dirac Model . . . . .	19

<b>5</b>	<b>Static and Dynamic Characterization</b>	<b>21</b>
5.1	Static Measurements . . . . .	21
5.2	Small Signal Modulation Response . . . . .	22
<b>6</b>	<b>Measurements of Eye Diagram and BER</b>	<b>27</b>
6.1	Back-to-Back . . . . .	28
6.2	Transmission over Optical Fiber . . . . .	32
6.3	Back-to-Back Using a Limiting Receiver . . . . .	33
<b>7</b>	<b>Measurements of Timing Jitter</b>	<b>35</b>
7.1	Back-to-Back . . . . .	38
7.2	Impact of Using Higher Modulation Amplitude . . . . .	40
7.3	Comparison of Jitter Performance . . . . .	42
7.4	Transmission over Optical Fiber . . . . .	44
7.5	Impact of Using a Limiting Receiver . . . . .	46
<b>8</b>	<b>Conclusion</b>	<b>49</b>
	<b>Bibliography</b>	<b>51</b>
<b>A</b>	<b>Small Signal Modulation Response</b>	<b>55</b>
<b>B</b>	<b>Eye Diagrams of the Modulation Signal</b>	<b>57</b>
<b>C</b>	<b>Timing Jitter</b>	<b>59</b>

# Chapter 1

## Introduction

The demand for higher data rates is increasing rapidly. The large increase in Internet traffic, e.g. streaming video, social networking and cloud storage, has increased the demands of high-capacity links between servers in data centers [1]. The same demand for higher data rates also applies to high-performance computing (HPC) systems, which depend on high-speed interconnects between multiple servers [2]. To meet the demand for higher transmission speeds, there is a trend to replace electrical interconnects with optical ones. This is due to that electrical interconnects becomes impractical already at 10 Gbit/s for transmission distances longer than a few meters, due to their bulky size and high attenuation at high frequencies. The high attenuation increases the error rates, which means that more power is needed to overcome the attenuation and error correction schemes are required [1, 3–7].

Besides high-speed capabilities, another major advantage for the optical interconnects is the potential for high efficiency, i.e. that the power consumption can be low, which of course is important from an environmental point of view [2]. For short-reach communication like optical interconnects, it is possible to use multimode fibers (MMF) and multimode lasers. This makes the vertical-cavity surface-emitting laser (VCSEL) an attractive option, due to the potential for low-cost fabrication, energy-efficient operation, and excellent high-speed properties at low currents [8].

A lot of work has been done to improve the bandwidth of 850 nm VCSELs for use in short-reach optical links [8, 9]. 850 nm is the industry standard wavelength for optical interconnects and this is where high-speed MMF is available. Recent work at the Photonics Laboratory at Chalmers has shown that the high-speed performance depends strongly on the photon lifetime, which is related to the mirror reflectivity [10]. An investigation by P. Westbergh et al. have highlighted that there exists an optimum photon lifetime which will give rise to the highest small signal modulation bandwidth for a particular VCSEL [11]. The optimum exists because of a trade-off between high differential gain and low damping, which can be fine-tuned by optimizing the photon lifetime. Using an empirically found optimum photon lifetime for maximized bandwidth,

they were able to transmit error-free at a data rate of 47 Gbit/s back-to-back (BTB) and 44 Gbit/s over 50 m of OM4 fiber [12], the highest data rates reported for VCSELs of any wavelength without equalization operating at room temperature. By *using equalization*, IBM recently demonstrated a VCSEL-based link operating at record high data rates up to 56.1 Gbit/s [13]. These results should be compared with the current commercially available VCSELs which transmit at around 10 Gbit/s [8], although at least one vendor is providing sample VCSELs operating at 20 Gbit/s [14].

The optical signal used for data transmission is obtained by large signal modulation of the VCSEL (usually on-off keying, OOK). Since it is not certain that the damping (induced by a certain photon lifetime) optimized for high small signal bandwidth corresponds to the damping best suited for high-speed data transmission, the impact of the damping on transmission speed needs further study.

## 1.1 Purpose and Objective

The purpose of this work is to further study the impact of the damping on the high-speed properties of the 850 nm VCSEL, in particular through large signal experiments and timing jitter analysis. The analysis of the experimental data should provide a deeper understanding of the performance limits and trade-offs associated with the damping and its impact on the data transmission properties. The goal of the work is to contribute to an improvement of the data transmission speed of the VCSEL.

## 1.2 Scope

The work primarily consisted of transmission experiments, where the influence of the damping on the VCSEL's ability to transmit data was studied. The transmission experiments were performed with the standard modulation format OOK using direct modulation. Some static and dynamic characterization was also performed to be able to compare with previous results in e.g. [11, 12]. All measurements were made at room temperature.

## Chapter 2

# Static Operation of VCSELs

A laser is a light emitting device based on stimulated emission. Experimentally, it was first demonstrated by T. Maiman in 1960 [15]. All lasers consists of a gain medium inside a cavity (an optical resonator often consisting of two semitransparent mirrors). Lasing can occur if sufficient amount of energy is supplied to the gain medium (through pumping) and if the light field repeats itself in both phase and magnitude after one round trip in the cavity. This chapter treats the basic operation of a VCSEL.

### 2.1 Semiconductor Laser

The typical semiconductor laser uses a forward biased *pin*-junction as a gain material. To confine carriers in the active (intrinsic) region, the *p*- and *n*-regions consist of semiconductor material with larger band gap. The electrical carriers (electrons and holes) will accumulate in the active region during forward bias, which means that the carriers can interact with photons through stimulated emission. At a certain current, called the threshold current, the gain induced by the accumulated carriers will equal the cavity losses (internal and mirror losses) and lasing will start. The material gain needed to reach threshold is referred to as the amplitude condition and states that the amplitude of the field must be the same after one round-trip and is given by [16]

$$g_{\text{th}} = \frac{1}{\Gamma} [\alpha_i + \alpha_m] = \frac{1}{\Gamma} \left[ \alpha_i + \frac{1}{2L} \ln \left( \frac{1}{R_1 R_2} \right) \right], \quad (2.1)$$

where  $\Gamma = V_a/V_p$  is the confinement factor (the overlap between the active region and the optical field, where  $V_a$  is the active region volume and  $V_p$  the volume of the lasing mode),  $\alpha_i$  the internal loss,  $\alpha_m$  the mirror loss,  $L$  the cavity length, and  $R_1$  and  $R_2$  the power reflectivities of the mirrors. At currents above the threshold the excess carriers injected to the active region are consumed by stimulated emission. This means that the carrier concentration and gain is clamped at their threshold levels and the output power

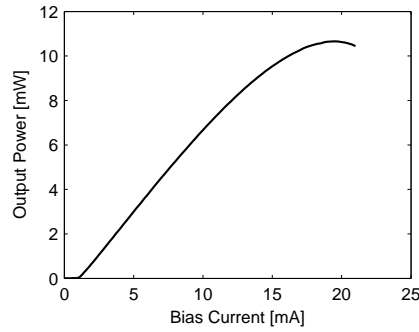


**Figure 2.1:** Example of the relation between current and optical output power.

increases with current above threshold. Eventually thermal effects will cause the output power to reach the roll-over, which will limit the maximum output power. An example of a typical relation between current and optical output power can be seen in figure 2.1.

There is along with the amplitude condition also a phase condition, which states that the phase of the field must be repeated after one round-trip [16]

$$\exp\left(-j\frac{2\pi}{\lambda_0/n_{\text{eff}}}\cdot 2L\right) = 1 \quad \Rightarrow \quad \lambda_0 = \frac{2Ln_{\text{eff}}}{m}, \quad (2.2)$$

where  $\lambda_0$  is the vacuum wavelength,  $n_{\text{eff}}$  the effective refractive index, and  $m$  an integer number. The phase condition in (2.2) states that only a discrete number of resonances, referred to as longitudinal modes, exists in the cavity. However, only resonances overlapping with the gain spectrum, i.e. that may fulfill the amplitude condition, can lase.

## 2.2 Vertical-Cavity Surface-Emitting Laser

The most straight forward realization of a semiconductor laser is the edge emitting laser where the longitudinal cavity is defined by edges obtained by cleaving. The cleaved facets will then act as mirrors due to the high index-contrast between the semiconductor and air. This means that the lasers need to be cut apart from each other in order to be tested. The vertical-cavity surface-emitting laser has a cavity oriented orthogonal to the surface, which means that the light is emitted perpendicular to the surface. This is useful for on-wafer testing, which can be done without any cutting. The cavity of a VCSEL is usually short, in the order of the wavelength  $\lambda$ , which is in the order of a micrometer.

The VCSELS used in this study are from the third generation of high-speed VCSELS fabricated at Chalmers and are presented in more detail in [12]. The  $\lambda/2$  long cavity is formed by two distributed Bragg reflectors (DBR) working as mirrors; one at the top and one at the bottom. A DBR is a stack of  $\lambda/4$ -layers consisting of alternating high and low refractive index. The active region providing the gain consists of five

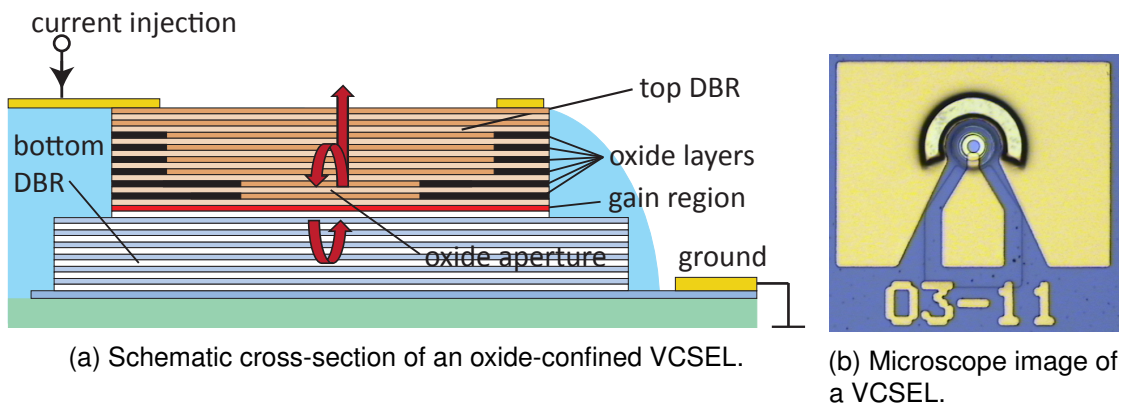


**Figure 2.2:** Schematic figure and microscope image of a VCSEL.

strained  $\text{In}_{0.10}\text{Ga}_{0.90}\text{As}/\text{Al}_{0.37}\text{Ga}_{0.63}\text{As}$  quantum wells, while electrical and transverse optical confinement is obtained by the use of oxide apertures. Only one oxide aperture is needed for optical and electrical confinement, but more are included to reduce the parasitic capacitance of the device to improve high-speed performance. A schematic cross-section of the VCSEL can be seen in figure 2.2(a) and a microscope image of a fully processed VCSEL on wafer in figure 2.2(b).



## Chapter 3

# Dynamic Operation of VCSELs

The dynamic properties of a VCSEL can be described by rate equations, which are presented in the section below. From these equations a small signal model can be derived, as presented in section 3.2. The influence of damping on the dynamic properties and how it can be tuned is briefly described in 3.3.

### 3.1 Rate Equations

The dynamic relationship between carriers and photons in a laser is usually modeled by two coupled rate equations; one equation for the carrier density, and one for the photon density. Charge neutrality requires the density of electrons and holes to be equal, hence only one equation for the carrier density is needed. While this description holds for a single mode laser, multi mode lasers strictly need one rate equation for every lasing mode. The behavior of highly multimode oxide confined VCSELs are, however, similar to a single mode laser despite of being multimode, since the modes have a high transverse overlap. This means that as long as the total power is considered it is sufficient to only use two rate equations, which are [17]

$$\frac{dN}{dt} = \frac{\eta_i I}{qV_a} - (A_r N + B_r N^2 + C_r N^3) - v_g G S, \quad (3.1)$$

$$\frac{dS}{dt} = \Gamma v_g G S - \frac{S}{\tau_p} + \Gamma \beta B_r N^2, \quad (3.2)$$

where  $N$  is the excess carrier density in the active region,  $\eta_i$  the internal quantum efficiency (the fraction of injected current that generate carriers in the active region),  $I$  the injected current,  $q$  the elementary charge,  $V_a$  the active region volume,  $A_r N + B_r N^2 + C_r N^3$  is the recombination rate from spontaneous and non-radiative recombination ( $A_r$  is the Shockley-Read-Hall recombination coefficient,  $B_r$  the spontaneous emission coefficient, and  $C_r$  the Auger recombination coefficient, where the subscript r refers to recombination),

$v_g$  the group velocity of the lasing mode,  $G$  the material gain,  $S$  the photon density of the lasing mode,  $\Gamma$  the confinement factor,  $\tau_p$  the photon lifetime, and  $\beta$  is the fraction of photons generated by spontaneous emission which are coupled into the lasing mode.

The fact that the gain saturates at high photon densities is accounted for by [18]

$$G = G(N, S) = \frac{g(N)}{1 + \varepsilon S},$$

where  $\varepsilon$  is the gain compression factor. Except from steady-state solutions, no analytical solutions exists to the rate equations (3.1) and (3.2), but if the analysis is limited to small perturbations from the steady-state solution, a small signal analysis can be performed.

### 3.2 Small Signal Analysis

By using Taylor expansion of the first order on the perturbations, the following substitutions can be made

$$\begin{aligned} I &= I_b + \delta I, \\ N &= N_b + \delta N, \\ S &= S_b + \delta S, \\ G(N, S) &= \frac{g_b}{1 + \varepsilon S} + \frac{g_0}{1 + \varepsilon S} \delta N - \frac{\varepsilon G}{1 + \varepsilon S} \delta S, \end{aligned}$$

where the subscript b denotes a linearization at a bias point  $I_b$  above threshold.  $g_b$  is the gain at the bias point and since the gain is clamped at threshold,  $g_b$  equals the threshold gain  $g_{th}$ .  $g_0$  is the nominal differential gain  $\frac{\partial g}{\partial N}$  at the bias point (differential gain without gain compression). Setting the time derivatives of the steady-state quantities to zero, neglecting higher order terms and the spontaneous emission factor  $\beta$ , and using the steady-state relation (derived from (3.2))

$$\frac{1}{\Gamma \tau_p} = \frac{v_g g_b}{1 + \varepsilon S_b},$$

the small signal equations become [18]

$$\frac{d}{dt} \delta N = \frac{\eta_i}{q V_a} \delta I - \left[ \frac{1}{\tau_{\Delta N}} + \frac{v_g g_0 S_b}{1 + \varepsilon S_b} \right] \delta N - \left[ \frac{1}{\Gamma \tau_p} - \frac{v_g \varepsilon G S_b}{1 + \varepsilon S_b} \right] \delta S, \quad (3.3)$$

$$\frac{d}{dt} \delta S = \frac{\Gamma v_g g_0 S_b}{1 + \varepsilon S_b} \delta N - \frac{\Gamma v_g \varepsilon G S_b}{1 + \varepsilon S_b} \delta S, \quad (3.4)$$

where  $\tau_{\Delta N}$  is the differential carrier lifetime defined as

$$\frac{1}{\tau_{\Delta N}} = A_r + 2B_r N_b + 3C_r N_b^2.$$

Time derivation of (3.4) and insertion in (3.3) to get rid of  $\delta N$  yields a second order system [18]

$$\frac{d^2}{dt^2}\delta S + \gamma \frac{d}{dt}\delta S + 4\pi^2 f_r^2 \delta S = \frac{\eta_i}{qV_a} \frac{\Gamma v_g g_0 S_b}{1 + \varepsilon S_b} \delta I, \quad (3.5)$$

where the resonance frequency  $f_r$  and the damping factor  $\gamma$  can be written as

$$f_r^2 = \frac{1}{4\pi^2} \left[ \frac{1}{\tau_p} \frac{v_g g_0 S_b}{1 + \varepsilon S_b} + \frac{1}{\tau_{\Delta N}} \frac{\Gamma v_g \varepsilon G S_b}{1 + \varepsilon S_b} \right], \quad (3.6)$$

$$\gamma = \frac{v_g g_0 S_b}{1 + \varepsilon S_b} + \frac{\Gamma v_g \varepsilon G S_b}{1 + \varepsilon S_b} + \frac{1}{\tau_{\Delta N}}. \quad (3.7)$$

The second order system (3.5) contains the photon density, which can be related to the optical output power by

$$P_{\text{out}} = \eta_0 \frac{hcV_p}{\lambda_0 \tau_p} S,$$

where  $\eta_0$  is the optical efficiency (the fraction of light that couples out from the cavity), and  $V_p$  the volume of the lasing mode. The modulation response to a small sinusoidal current change  $\delta I(t) = \delta I_0 e^{j2\pi f t}$  is found by substitution of  $\frac{d}{dt}$  with  $j2\pi f$  in (3.5). Assuming  $\delta S(t) = \delta S_0 e^{j2\pi f t}$  and  $\delta P(t) = \delta P_0 e^{j2\pi f t}$  yields the following expression for the intrinsic transfer function [18]

$$H_i(f) = \frac{\delta P_0}{\delta I_0} = \eta_d \frac{hc}{\lambda_0 q} \cdot \frac{f_r^2}{f_r^2 - f^2 + j \frac{f}{2\pi} \gamma}, \quad (3.8)$$

where  $\eta_d = \eta_i \eta_0$  is the differential quantum efficiency and  $f_r$  has been approximated by

$$f_r \approx \frac{1}{2\pi} \sqrt{\frac{v_g g_0 S_b}{\tau_p (1 + \varepsilon S_b)}}, \quad (3.9)$$

since we can assume that  $\tau_p \ll \tau_{\Delta N}$  and  $g_0 \sim \Gamma \varepsilon G$ .

### 3.2.1 Damping

The damping factor in (3.7) can be simplified by using the approximation for  $f_r$  in (3.9) [18]

$$\gamma \approx K \cdot f_r^2 + \gamma_0, \quad (3.10)$$

where  $\gamma_0 = \frac{1}{\tau_{\Delta N}}$  is the damping factor offset and  $K$  is the  $K$ -factor defined as

$$K = 4\pi^2 \left[ \tau_p + \frac{\varepsilon}{v_g g_0} \right]. \quad (3.11)$$

From (3.9) and (3.10) the intrinsic damping limitation can be found. The resonance frequency  $f_r$  increases as the photon density is increased, but the damping  $\gamma$  is also increased. Since the damping increases faster ( $\gamma \propto f_r^2 \propto S_b$ ) than the resonance frequency ( $f_r \propto \sqrt{S_b}$ ), the damping will eventually limit the system. This means that the maximum intrinsic 3 dB bandwidth is set by the  $K$ -factor and  $\gamma_0$ .

### 3.2.2 Bandwidth

The 3 dB bandwidth of the modulation response is defined by

$$\frac{|H_i(f_{3\text{ dB}})|^2}{|H_i(0)|^2} \equiv \frac{1}{2},$$

which means that the maximum intrinsic 3 dB bandwidth can be found by solving the following equation system

$$\begin{cases} \frac{|H_i(f_{3\text{ dB}})|^2}{|H_i(0)|^2} \equiv \frac{1}{2} \\ \frac{d(|H_i(f_{3\text{ dB,max}})|^2)}{d(f_r^2)} = 0 \end{cases}$$

which yields [18]

$$f_{3\text{ dB,max}} \approx \frac{2\sqrt{2}\pi}{K} - \frac{\gamma_0}{2\sqrt{2}\pi}. \quad (3.12)$$

This intrinsic bandwidth is typically  $>30$  GHz. However, it is difficult to reach due to effects from self-heating and electrical parasitics which typically are limiting the modulation bandwidth for a VCSEL.

### 3.2.3 $D$ -Factor

An important figure of merit for devices is the  $D$ -factor, which quantifies the increase of resonance frequency with current. A high  $D$ -factor is desired to enable high-speed modulation at low bias currents. The  $D$ -factor is defined as [18]

$$D \equiv \frac{f_r}{\sqrt{I_b - I_{\text{th}}}} = \frac{1}{2\pi} \sqrt{\frac{\eta_i \Gamma v_g g_0}{q V_a}}, \quad (3.13)$$

where  $I_{\text{th}}$  is the threshold current and the following relation has been used

$$\frac{S_b V_p}{\tau_p} = \frac{S_b V_a}{\Gamma \tau_p} = \eta_i \frac{I_b - I_{\text{th}}}{q}.$$

It should be noted that the gain compression (in (3.9)) have been left out in (3.13), which means that the  $D$ -factor has to be evaluated at low currents where the equation is valid.

### 3.2.4 Electrical Parasitics

Electrical parasitics can be accounted for by an  $RC$ -filter modeled as an extra pole with cut-off frequency  $f_p$  [18]

$$H_{\text{par}}(f) = \frac{1}{1 + j \frac{f}{f_p}}.$$

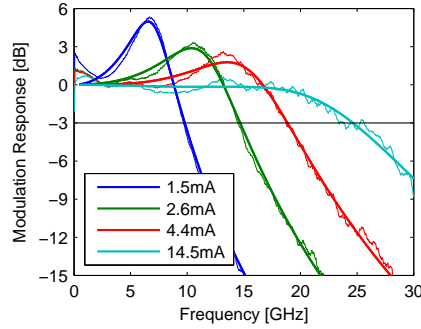


**Figure 3.1:** Example of a small signal modulation response.

Together with the intrinsic transfer function the total transfer function becomes

$$H(f) = |H_i(f) \cdot H_{\text{par}}(f)|^2 = A \cdot \left| \frac{f_r^2}{f_r^2 - f^2 + j\frac{f}{2\pi}\gamma} \cdot \frac{1}{1 + j\frac{f}{f_p}} \right|^2, \quad (3.14)$$

where  $A$  is an amplitude factor accounting for the slope efficiency of the laser, the dynamic response of the photodetector and the insertion loss of the microwave probe. An example of a measured small signal modulation response can be seen in figure 3.1.

### 3.3 Tuning the VCSEL Damping

As mentioned above, the damping limit can not be reached in practice due to the electrical parasitics and thermal effects. Nonetheless, a proper amount of damping is important as low damping will allow for the resonance peak to help push the bandwidth to higher values. However, even though high damping will decrease the bandwidth, it will also flatten the frequency response, which could be beneficial for data transmission purposes. The damping factor in (3.10) is mostly affected by the  $K$ -factor in (3.11), which in turn is partly dependent on the photon lifetime  $\tau_p$ . The photon lifetime is dependent on the reflectivity of the mirrors; a high reflectivity gives a high photon lifetime and vice-versa. This means that a low damping requires the reflectivity to be rather low (but still above 95%), while for a high damping the reflectivity should be larger (typically around 99%) [18].

The reflectivity of the top mirror is greatly influenced by the thickness of the uppermost DBR-layer. This is due to that the large refractive index difference at the interface between semiconductor and air will induce a reflection with rather large amplitude while the thickness of the layer will affect the phase of that last reflection. If the last reflection is in phase with the rest of the reflections between the DBR-layers, the reflectivity of the mirror will have a maximum, while if it is out of phase with the rest of the DBR-layers the reflectivity will have a local minimum. The maximum will occur if the thickness of

the last DBR-layer is  $\lambda/4$  while the minimum will occur if the thickness is 0 or  $\lambda/2$ . The reflectivity can be fine-tuned by a shallow surface etch to obtain a certain photon lifetime and therefore a certain damping [18].

Since the VCSELS used in this work are fabricated with an anti-phase layer to allow for mode-filter integration, the thickness of the top layer is  $\lambda/2$ . An integrated mode-filter can be used to increase the losses for higher-order modes, which will reduce the spectral width of the VCSEL [19]. A VCSEL with an anti-phase layer will have rather low reflectivity for the output mirror, which will induce low damping. With a surface etch, the reflectivity and damping is increased and a maximum is obtained when all of the anti-phase layer is gone ( $\lambda/4 = 59$  nm etch). This allows for the photon lifetime to be tuned between  $\sim 0.5$  ps (out-of-phase reflection) and  $\sim 4.1$  ps (in-phase reflection) [12].

## Chapter 4

# Data Transmission

When the VCSEL is used for data transmission it is biased with a certain DC current. The optical data signal is obtained by adding a modulation signal to the laser. The signal consists of a large amount of ones and zeros (high and low voltages), and transitions between these levels correspond to a voltage step change. When a voltage step is applied to a semiconductor laser it will take some time for the laser to rise or fall to this new level (rise and fall times) and then there will be relaxation oscillations around the final level. The relaxation oscillations, and to some extent also rise and fall times, will induce timing jitter in the system. In this chapter bit error rate, eye diagram, timing jitter, and techniques to extract jitter parameters will be treated.

### 4.1 Bit Error Rate

To be able to use the VCSEL as a data transmitter the errors in the received signal need to be very few. This is quantified by the bit error rate (BER), which is the probability that the received bit is erroneous. Typically, optical systems require a BER of less than  $10^{-12}$ , which often is called error-free. In this work a BER of  $5 \cdot 10^{-13}$  has been required to ensure that the BER is below  $10^{-12}$  and therefore error-free. Empirically, the BER is calculated as the number of erroneous bits over the number of received bits, but since errors occur quite seldom at low probabilities ( $< 10^{-9}$ ) the use of statistics is necessary for reasonable measurement duration. The number of transmitted bits,  $N_{\text{bits}}$ , detected without any error required to ensure a bit error rate below  $p$  with a statistical confidence of  $c$  is given by [20]

$$N_{\text{bits}} = -\frac{\ln(1-c)}{p}. \quad (4.1)$$

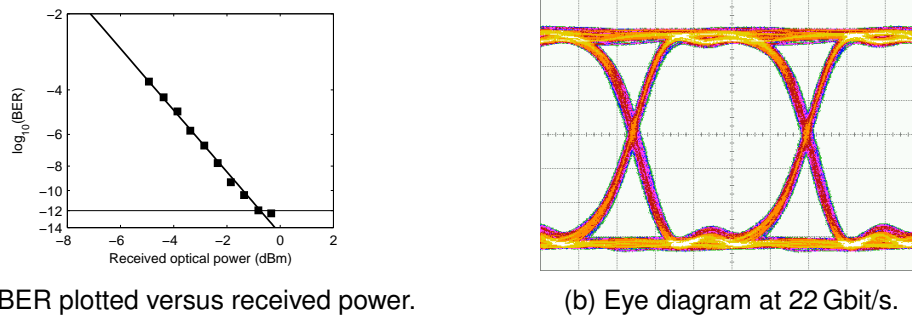


**Figure 4.1:** Examples of BER plotted versus received optical power and an eye diagram.

A statistical confidence of 95% is typically required. Using this level of statistical confidence, a measurement of a BER below  $5 \cdot 10^{-13}$  require that  $6 \cdot 10^{12}$  bits are received without any error. This corresponds to a measurement time of 10 and 2 min using the bit rates 10 and 50 Gbit/s, respectively.

To show that a laser can transmit data error-free at a certain data rate, it is common to measure the sensitivity, i.e. BER versus received optical power. The BER will be larger for lower power and lower for higher power. The logarithm of the BER is then plotted (using a logarithmic axis) against the received optical power in dBm, which will ideally form a straight line. An example of a plot of BER versus received power can be seen in figure 4.1(a).

## 4.2 Eye Diagram

The eye diagram, which is an overlay of the signal waveform, can be recorded with an oscilloscope and used to quickly observe indications of the signal quality. The ideal eye diagram has sharp and fast transitions between ones and zeros in narrow transition regions with large difference between the levels, i.e. large signal amplitude. This will give an open eye diagram, while the introduction of wider transition regions or smaller signal amplitude will introduce closing of the eye diagram in either the time or the amplitude domain. An example of an eye diagram can be seen in figure 4.1(b).

## 4.3 Timing Jitter

To obtain the lowest possible BER it is important to be able to sample the data at the ideal position (time delay) in the bit slot. Unfortunately, the timing of the data transitions forming the bit slot are deviating from their intended (or ideal) positions, making the time slot for sampling shorter. This phenomena is called timing jitter, often only referred to as jitter. The result of jitter is that the eye diagram is closed in the time domain [21, 22].

The relaxation oscillations and the rise and fall times of the laser, discussed in the beginning of this chapter will contribute to the jitter. Since the damping of the VCSEL will influence both relaxation oscillations and rise/fall times, it is interesting to investigate the jitter to find out how the damping is affecting the data transmission abilities of the studied VCSELs.

Jitter can be divided in two subcategories; random jitter which is unbounded and uncorrelated to the data, and deterministic jitter which is bounded and can be correlated to the data.

### 4.3.1 Random Jitter

Random jitter (RJ) is caused by small uncorrelated jitter components which add up. These jitter components are mostly due to noise in the electrical domain. The noise is dominated by thermal noise which has a Gaussian distribution. Other components with other distributions (like shot noise) can also contribute to the RJ, but it will still obtain a Gaussian distribution, since many small uncorrelated random components will add up to a Gaussian distribution due to the central limit theorem. Since a Gaussian random variable in principle can obtain arbitrary large values, RJ is referred to as unbounded jitter [21, 23, 24].

### 4.3.2 Deterministic Jitter

The name deterministic jitter (DJ) implicates that the jitter behavior can (in principle) be predicted. This is the reason DJ is bounded in amplitude. DJ itself consists of a finite number of deterministic jitter components. These deterministic jitter components can be divided into different types of deterministic jitter; duty cycle distortion, data dependent jitter and bounded uncorrelated jitter [21, 24].

#### Duty Cycle Distortion

Duty cycle distortion (DCD) is correlated to the data. It is caused by ones and zeros having different pulse widths, i.e. the duration of a one is different from a zero. This can be caused by the signal having different rise and fall times or that the sampling of the signal is performed at an amplitude threshold shifted from the ideal one [21, 24].

#### Data Dependent Jitter

Jitter that varies depending on the particular data is called data dependent jitter (DDJ). It can be caused by inter symbol interference (ISI) due to dispersion effects or from bandwidth limitations in the transmitter or any other part of the system, i.e. transmission

media, receiver, etc. Reflections due to imperfect impedance matching or improper optical coupling can also cause DDJ, since that also will limit the bandwidth [21, 24]. This means that DDJ is affected when the data rate is increased, due to that a signal with increased data rate includes higher frequency components, which will be more affected by bandwidth limitations in the studied system.

### Bounded Uncorrelated Jitter

Jitter sources that not are aligned to the data are called bounded uncorrelated jitter (BUJ). It is caused by noise in the power supply that is affecting the transmitted signal or noise from other sources than the ones under test. It can also be caused by crosstalk or an applied sinusoidal jitter included in the signal to test its robustness against noise. Since this study is only performed with one channel without any external jitter added on purpose, BUJ can be assumed to have limited effect [21, 24].

### 4.3.3 Total Jitter

The total jitter (TJ) is the result of all jitter components. Since it includes both unbounded (i.e. RJ) and bounded (i.e. DJ) it is crucial that it is calculated at a specific BER (TJ(BER)). This is due to that a requirement on lower BER will increase the influence of RJ and therefore increase the TJ. It is common that a BER of  $10^{-12}$  is required, e.g. in Fibre Channel [21], and therefore it will be taken as a definition in the remainder of this thesis that

$$\text{TJ} = \text{TJ}(\text{BER} = 10^{-12}). \quad (4.2)$$

The eye opening at a certain BER can be calculated as the time duration of the bit slot minus the total jitter at that BER. If BER of  $10^{-12}$  is required for this parameter as well, it can be written like [25]

$$\text{Eye opening} = T_b - \text{TJ}(\text{BER} = 10^{-12}), \quad (4.3)$$

where  $T_b$  is the time duration of the bit slot ( $T_b = 1/B$ , where  $B$  is the bit rate).

The total jitter can be given in absolute units, i.e. width of the jitter in time domain, or in relative units, called unit intervals (UI). The total jitter given in relative units,  $\text{TJ}_{\text{rel}}$ , is given by

$$\text{TJ}_{\text{rel}} = \frac{\text{TJ}_{\text{abs}}}{T_b}, \quad (4.4)$$

where  $\text{TJ}_{\text{abs}}$  is the total jitter in absolute units.

## 4.4 The Dual-Dirac Model

To be able to extract the different jitter parameters from measured jitter and extrapolate to low BER and find the total jitter, the use of models is necessary. Quite a few models exist in the literature, depending on the measurement technique used. One of the earliest models, called Tailfit, was developed by Wavecrest Corporation [26]. Tailfit exploits the fact that the jitter histogram tails, obtained between symbols using an oscilloscope, are Gaussian. These tails are fitted to the Tailfit model to extract the jitter parameters.

The model chosen for this work is the dual-Dirac model since it is a fairly simple model and can be used with data obtained from BER measurements. The dual-Dirac model was originally developed for Fibre Channel [21], and is used in the specification of industry standards like Ethernet [27], PCI Express, and FB DIMM [28]. It basically consists of the convolution between a Gaussian function and two Dirac-delta functions. In the following, the dual-Dirac model and a procedure to fit measured data to it is presented.

The probability density function (PDF) for the deterministic jitter  $J_{DJ}(t)$  can be represented by two Dirac delta functions,  $\delta(t)$ , separated in time by the peak-to-peak value of the deterministic jitter,  $DJ = \mu_L - \mu_R$  [21, 29]

$$J_{DJ}(t) = \frac{1}{2} [\delta(t - \mu_R) + \delta(t - \mu_L)], \quad (4.5)$$

where the subscripts L and R denotes the left and right side of the crossing. The PDF for the random jitter  $J_{RJ}(t)$  can be modeled as a Gaussian function with standard deviation  $\sigma_R$  and  $\sigma_L$ , respectively [21]

$$J_{RJ}(t) = \frac{1}{\sqrt{2\pi}\sigma} \exp\left[-\frac{t^2}{2\sigma^2}\right]. \quad (4.6)$$

The total jitter PDF  $J_{TJ}(t)$  can be obtained by convolution of the DJ PDF and the RJ PDF [21]

$$\begin{aligned} J_{TJ}(t) &= J_{DJ}(t) * J_{RJ}(t) \\ &= \frac{1}{2\sqrt{2\pi}} \left\{ \frac{1}{\sigma_R} \exp\left[-\frac{(t - \mu_R)^2}{2\sigma_R^2}\right] + \frac{1}{\sigma_L} \exp\left[-\frac{(t - \mu_L)^2}{2\sigma_L^2}\right] \right\}. \end{aligned} \quad (4.7)$$

The BER at the left and right side of the crossing is then given by the cumulative distribution function (CDF) at their respective sides

$$\text{BER}_L(t) = \rho_L \int_{-\infty}^t J_{TJ}(\tau) d\tau, \quad (4.8)$$

$$\text{BER}_R(t) = \rho_R \int_t^{\infty} J_{TJ}(\tau) d\tau, \quad (4.9)$$

where  $\rho_L$  and  $\rho_R$  are the average transition densities, i.e. the ratio of logic transitions to the total number of transmitted bits. For a pseudo random bit sequence (PRBS), which is used in this work, the density is 0.5 for both  $\rho_L$  and  $\rho_R$ .

By inserting the TJ PDF from (4.7) into the right side BER in (4.8) the following is obtained

$$\begin{aligned} \text{BER}_R(t) &= \rho_R \int_{\tau=t}^{\infty} J_{\text{TJ}}(\tau) d\tau \\ &= \frac{\rho_R}{\sqrt{2\pi} \sigma_R} \int_{\tau=t}^{\infty} \exp\left[-\frac{(\tau - \mu_R)^2}{2\sigma_R^2}\right] d\tau. \end{aligned} \quad (4.10)$$

The equation can be further simplified by using the following variable substitution

$$\begin{aligned} x = \frac{\tau - \mu_R}{\sqrt{2} \sigma_R} &\quad \implies \quad \tau = \sqrt{2} \sigma_R x + \mu_R, \\ \frac{d\tau}{dx} = \sqrt{2} \sigma_R &\quad \implies \quad d\tau = \sqrt{2} \sigma_R dx, \end{aligned}$$

which gives that the integral in (4.10) finally becomes

$$\text{BER}_R(t) = \frac{\rho_R}{\sqrt{\pi}} \int_{x=\frac{t-\mu_R}{\sqrt{2}\sigma_R}}^{\infty} e^{-x^2} dx. \quad (4.11)$$

Since the complementary error function is given by [30]

$$\text{erfc}(t) = 1 - \text{erf}(t) = \frac{2}{\sqrt{\pi}} \int_{x=t}^{\infty} e^{-x^2} dx, \quad (4.12)$$

the integral in (4.11) can be written as

$$\text{BER}_R(t) = \frac{\rho_R}{2} \text{erfc}\left[\frac{t - \mu_R}{\sqrt{2} \sigma_R}\right]. \quad (4.13)$$

By performing an equivalent analysis for the left side, the following is obtained

$$\text{BER}_L(t) = \frac{\rho_L}{2} \text{erfc}\left[\frac{\mu_L - t}{\sqrt{2} \sigma_L}\right]. \quad (4.14)$$

These two equations, (4.13) and (4.14), can be rewritten on linear form which enables easier fitting to measured data [29]

$$\sqrt{2} \text{erf}^{-1}\left[1 - \frac{2 \text{BER}_R(t)}{\rho_R}\right] = \frac{t}{\sigma_R} - \frac{\mu_R}{\sigma_R}, \quad (4.15)$$

$$\sqrt{2} \text{erf}^{-1}\left[1 - \frac{2 \text{BER}_L(t)}{\rho_L}\right] = \frac{\mu_L}{\sigma_L} - \frac{t}{\sigma_L}. \quad (4.16)$$

When the above equations are fitted to measured data,  $\mu_R$ ,  $\mu_L$ ,  $\sigma_R$  and  $\sigma_L$  are obtained and can be used to calculate the root-mean-square (RMS) value of the random jitter and the peak-to-peak (pp) value of the deterministic jitter [29]

$$\text{RJ} = \text{RJ}_{\text{RMS}} = \frac{\sigma_R + \sigma_L}{2}, \quad (4.17)$$

$$\text{DJ} = \text{DJ}_{\text{pp}} = \mu_R - \mu_L. \quad (4.18)$$

In this work all values for RJ are given as root-mean-square while values for DJ are given as peak-to-peak, and will therefore only be referred to as RJ and DJ. The total jitter at a specific BER can then be calculated using [29]

$$\text{TJ}(\text{BER}) = \alpha(\text{BER}) \text{RJ} + \text{DJ}, \quad (4.19)$$

where

$$\alpha(\text{BER}) = 2\sqrt{2} \operatorname{erfc}^{-1}(2 \text{BER}) = \left\{ \text{BER} = 10^{-12} \right\} \approx 14.069. \quad (4.20)$$

In this work all TJ values are calculated at a BER of  $10^{-12}$ , as mentioned in section 4.3.3. The value for  $\alpha(\text{BER} = 10^{-12})$  calculated above is a quite large value, which means that the effect of RJ on TJ is rather large.

#### 4.4.1 Limitations of the Dual-Dirac Model

It should be noted that the dual-Dirac model has received some criticism for underestimating DJ and overestimating RJ, for example in [31–33]. This is due to the assumptions made when using the dual-Dirac model, which is that jitter can be separated into RJ and DJ. It is also assumed that RJ follows a Gaussian distribution only characterized by the root-mean-square value of RJ, while DJ has a bounded distribution, which can be characterized by two Dirac-delta functions. These assumptions makes the model quite simple and easily fitted to measured data, but it risks sacrificing some of the physical meaning of the jitter parameters. The assumption of Gaussian RJ is quite accurate, but DJ can be quite different than the assumption in the model. However, as long as the extracted values for RJ, DJ and TJ is only compared with other values extracted using the same model, the comparisons will be accurate enough [34].



## Chapter 5

# Static and Dynamic Characterization

To study the impact of damping on data transmission abilities, four VCSELs with 8  $\mu\text{m}$  oxide aperture diameter were chosen from four chips with different shallow surface etch depths. The chips have been cleaved apart from the same  $\sim 1 \times 1$  cm chip, after the VCSEL fabrication, to be able to etch the surfaces different amounts. The different etch depths results in different photon lifetimes (and therefore also damping) of the VCSELs, since the reflectance of the top mirror is largely influenced by the phase of the reflection in the semiconductor-air interface, as described in section 3.3. In table 5.1 there is a summary of static characteristics for the VCSELs used. In the following, the technique for static and dynamic characterization is described together with some measurement results acquired at room temperature.

### 5.1 Static Measurements

It is useful to know the statical properties of the VCSELs to be able to choose the correct bias points etcetera. By probing the VCSELs and sweeping the bias currents, the voltage across the VCSELs and the optical output power can be measured as function of current.

**Table 5.1:** Summary of the VCSELs used.

VCSEL	Etch depth [nm]	$I_{\text{th}}$ [mA]	$P_{\text{opt,max}}$ [mW]	Internal ref.no
A	0	1.71	10.0	51B2-1105
B	$\sim 28$	1.34	12.4	51B2-0408
C	$\sim 37$	1.09	10.7	51B2-0407
D	$\sim 45$	0.89	8.0	51B2-1108

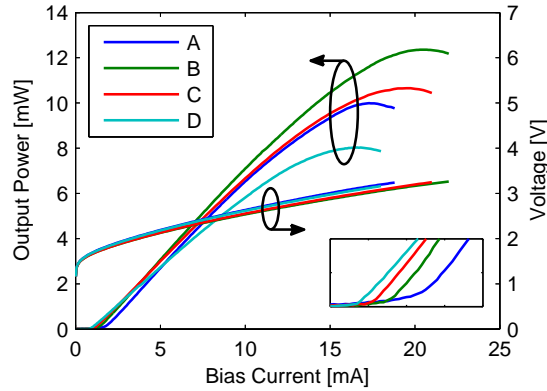


**Figure 5.1:** Output power and voltage versus bias current for VCSELs A–D. Inset: Zoom-in of the threshold region.

The optical power was measured with a large area silicon detector about 1 cm above the VCSELs to capture most of the light, while the voltage was measured with a voltage meter connected to the probe. The result of the measurements can be seen in figure 5.1. In the figure it is clear that VCSEL B has the highest maximum output power and that VCSEL D has the lowest threshold current. It can also be seen that the deeper the etch, the lower the threshold current. The reason for this is that deeper etch gives longer photon lifetime, i.e. reduced cavity losses, which means that the current needed for lasing is lower. The result clearly shows that the lasers used have different photon lifetimes, since the only device parameter that differs is the depth of the surface etch.

The optical spectrum of the VCSELs was measured by butt coupling the light into a short optical fiber connected to an optical spectrum analyzer (ANDO AQ6317B). The spectrum of the VCSELs at typical bias currents can be seen in figure 5.2, where it is obvious that the lasers are transversely multimode. Also included in the figures are the corresponding root-mean-square linewidths. It is interesting to note that the unetched laser (VCSEL A) does not lase at its fundamental mode at this bias current, which is an early indication of that it is not working very well, at least not for our purposes.

## 5.2 Small Signal Modulation Response

By measuring the small signal modulation response ( $S_{21}(f)$ ) of the VCSELs, insights about their high-speed performance can be gained by fitting the measured data to (3.14). The extracted parameters can then be used to estimate the  $K$ -factor together with the damping factor offset ( $\gamma_0$ ) in (3.10), and the  $D$ -factor in (3.13). To fit (3.14) to measured data, it is sufficient to only obtain the magnitude of the modulation response ( $|S_{21}(f)|$ ).

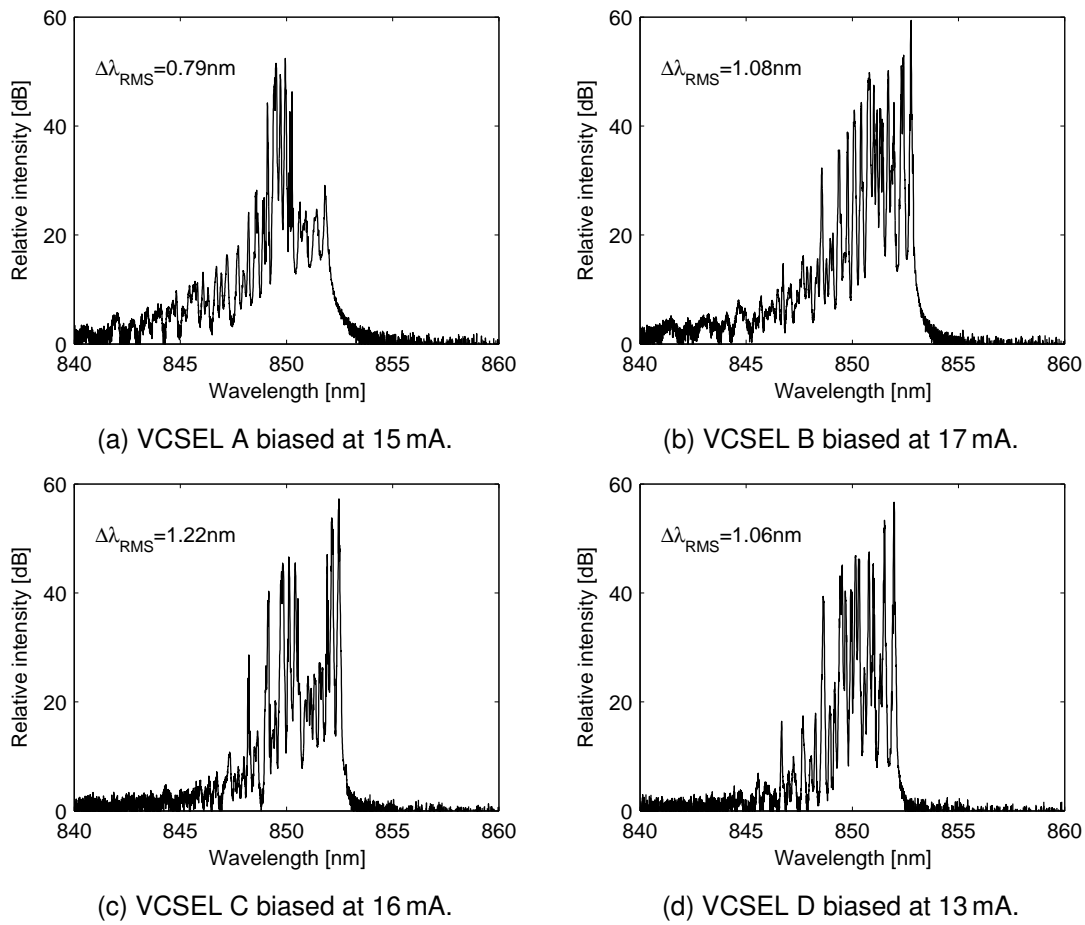


**Figure 5.2:** Measured spectrum for VCSELs with different etch depth.

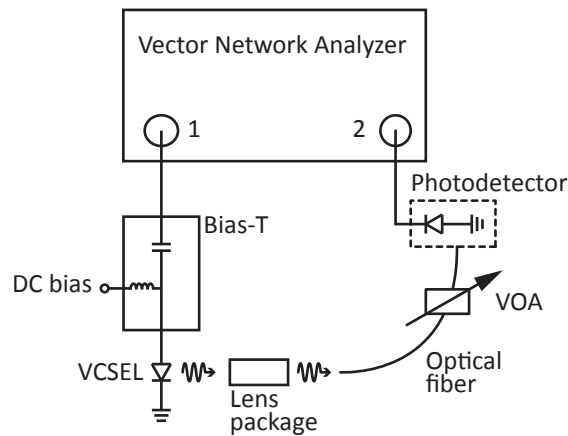
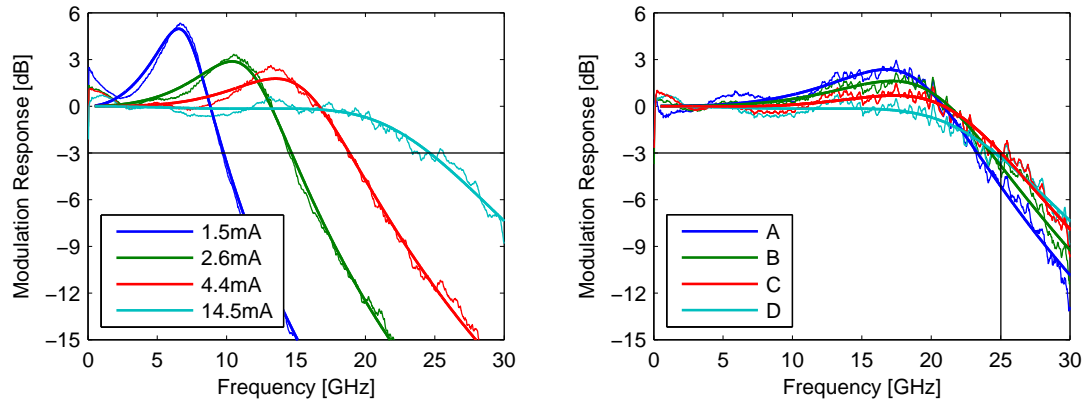


**Figure 5.3:** Measurement setup used for modulation response.



(a) Small signal modulation response of VCSEL D for different bias currents. The response at the largest bias current indicated correspond to the response with the maximum laser specific 3 dB bandwidth.  
 (b) Small signal modulation response of lasers with different etch depth at the bias current yielding the maximum laser specific 3 dB bandwidth.

**Figure 5.4:** Small signal modulation responses and corresponding fits to the transfer function.

The small signal modulation response was measured using an Anritsu 37397C 40 MHz–65 GHz vector network analyzer. The small signal sinusoidal modulation signal from port 1 of the network analyzer was combined with the bias current using a high frequency bias-T and was then applied to the VCSEL with a high-speed RF probe (Picoprobe 40A-GSG-100P from GGB industries). The VCSEL’s bondpad is designed to match the pitch of the ground-signal-ground probe. The modulated light from the VCSEL was coupled to a short (1 m long) 50  $\mu\text{m}$  multimode optical fiber using an anti-reflex coated lens package to obtain high coupling efficiency ( $>60\%$ ) and minimize optical feedback to the laser. The fiber was connected to an optical detector (New Focus 1481-S-50 25 GHz) via a JDSU OLA-54 variable optical attenuator (VOA), to reduce the optical power and keep the detector in its linear region, and another short (1 m long) optical fiber of the same type as the first one. The detector was connected to port 2 of the network analyzer. A schematic view of the setup can be seen in figure 5.3.

Before the modulation response was measured, the network analyzer required calibration. Since the network analyzer only was used to output a signal on port 1 and receive on port 2, and since only the magnitude response was measured, it was sufficient to only perform a thru calibration to remove the influence of the bias-T and the cables in the setup. The measured small signal modulation response data was then compensated for the insertion loss of the probe and the frequency response of the detector using calibration data provided from the respective manufacturers.

The measured small signal modulation response and corresponding fit for VCSEL D at selected bias currents is plotted in figure 5.4(a) while the responses and fits for VCSELs A–D at the bias currents that resulted in the highest 3 dB bandwidths are showed in

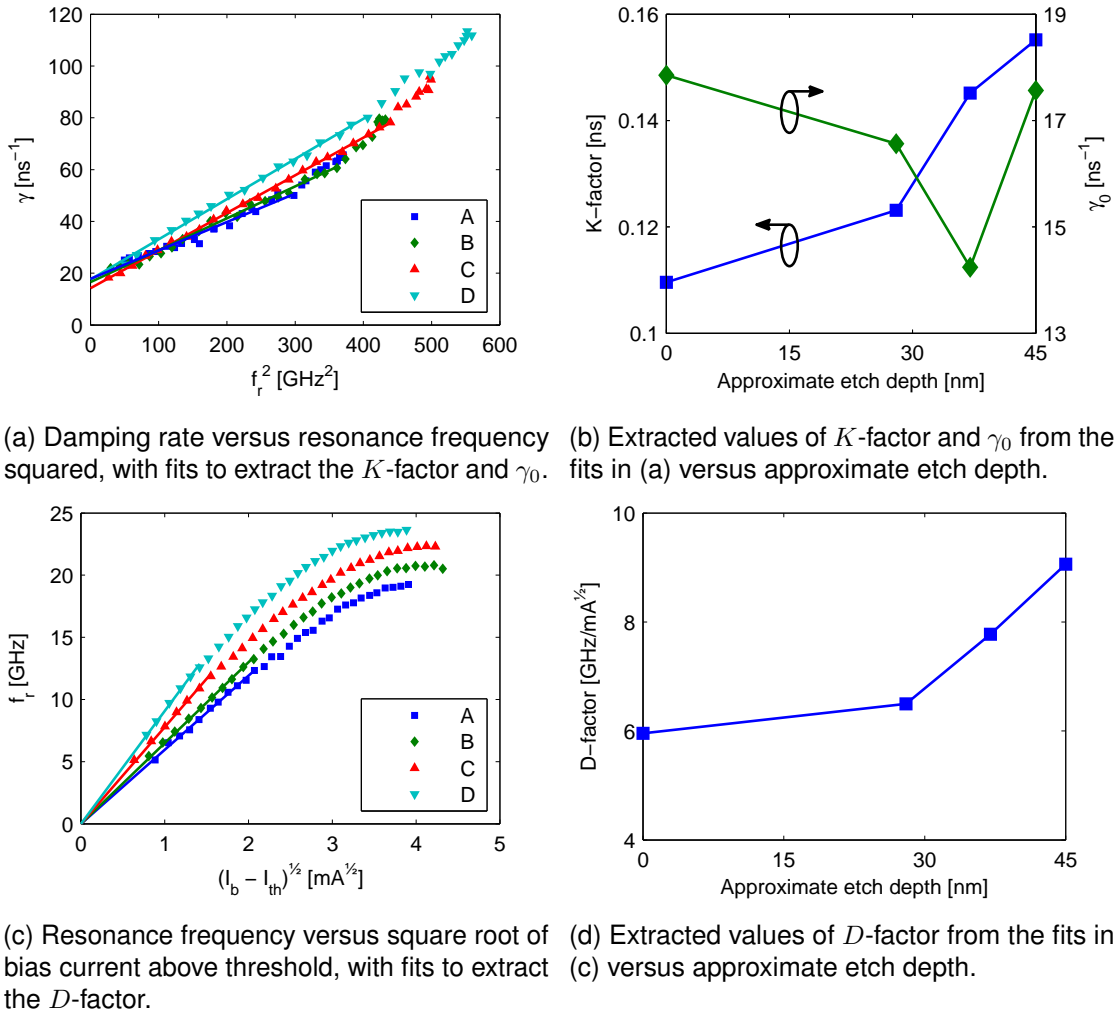


**Figure 5.5:** Fits and extracted values from the small signal modulation responses.

figure 5.4(b). It can be seen that VCSEL C has the highest 3 dB bandwidth of 25.0 GHz, and that VCSEL D is not far behind with a bandwidth of 24.6 GHz. VCSEL A and B reach 23.3 and 24.3 GHz, respectively. It is also interesting to note the response is most flat for VCSEL D which might indicate good data transmission performance. Modulation responses for VCSELs A–C like the one for VCSEL D in figure 5.4(a) are included in appendix A.

Plots showing the extraction of the  $K$ -factor, the damping offset  $\gamma_0$ , and the  $D$ -factor are to be seen in figure 5.5(a) and (c), while the extracted values are plotted versus approximate etch depth in figure 5.5(b) and (d). The highest  $K$ - and  $D$ -factor is obtained by VCSEL D, but that is also accompanied with a high damping offset  $\gamma_0$ . VCSEL C, however, has the lowest damping offset  $\gamma_0$  and only slightly lower  $K$ - and  $D$ -factor than VCSEL D, which is likely the reason behind VCSEL C's slightly higher 3 dB bandwidth than VCSEL D's.

## Chapter 6

# Measurements of Eye Diagram and BER

The small signal modulation response is only an indication of the VCSELs' high-speed performance in real data transmission applications, where large signal modulation is used. Usually, the large signal modulation changes abruptly between a low off-state (0) and a high on-state (1). These conditions were tested through transmitting non return to zero (NRZ) pseudo random bit sequences with word length  $2^7-1$ , from a bit pattern generator (SHF 12103A), amplified with a broadband amplifier (SHF 804 TL 22 dB) and attenuated with 13 dB (or 10 dB) RF attenuators and combined with the bias current in the bias-T, after which the data signal had an peak-to-peak amplitude of  $0.99 V_{pp}$  (or  $1.35 V_{pp}$ ). Eye diagrams of the data signal at different bit rates can be seen in appendix B. The signal was fed to the VCSEL using the same high-speed RF probe (Picoprobe 40A-GSG-100P) as in the small signal measurements. Using a lens package, the same as in the small signal measurements, the modulated light was coupled into a short multimode optical fiber (1 m long referred to as back-to-back) with  $50 \mu\text{m}$  core diameter, or longer OM4-fiber (50 or 100 m long), with a bandwidth distance product of  $4.7 \text{ GHz}\cdot\text{km}$ . The fiber was connected to the same variable optical attenuator as in the small signal measurements (JDSU OLA-54), connected to a photoreceiver through a short optical fiber (1 m long). The received optical power was monitored using the photoreceiver's DC-bias monitor function. Unless stated otherwise, the photoreceiver used was a New Focus 1484-A-50 22 GHz linear photoreceiver, which has a rather slow frequency roll off (33 GHz 6 dB bandwidth). Some measurements were also performed using a limiting photoreceiver (VI Systems R40-850 30 GHz) instead, since real systems often are designed for well defined levels of the ones and zeros. The photoreceiver was either connected to a sampling oscilloscope (Agilent Infiniium DCA-J 86100C), to be able to record eye diagrams and measure some statistical characteristics, or to an error analyzer (SHF 11100B) to be able to determine the BER. The bit pattern generator (BPG) and the error analyzer (EA) are together referred to as a bit error rate tester (BERT) and are in fact mounted

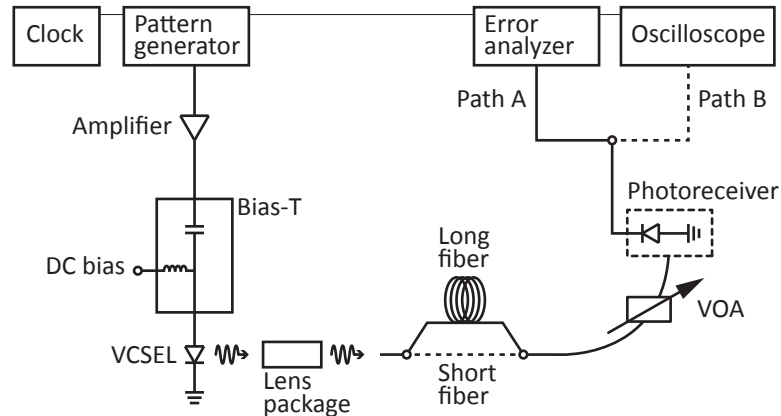


**Figure 6.1:** Measurement setup used for transmission experiments. Path A is used for BER measurements, while path B is used for eye recording.

in the same mainframe (SHF 10000C), which is connected to a computer via LAN to control the measurements. The BERT system used is specified to work at data rates up to 56 Gbit/s, but during the experiments the system worked up to 57 Gbit/s.

To be able to create the test pattern, the BPG required an external clock at half the data rate, which was generated with an RF synthesizer (Anritsu 69169A). Both the oscilloscope and the EA were synchronized with the BPG by a reference clock signal, which was retransmitted from the BPG clock output and connected to respective instrument's clock input. In real implementations, when the distance between transmitter and receiver is larger, the clock signal is required to be extracted from the data signal itself by so called clock recovery. An overview of the measurement setup can be seen in figure 6.1.

Eye diagrams were recorded with the variable optical attenuator set to 3 dB and enabled error-free data transmission, if not stated otherwise. The BER measurements were performed using as high optical attenuation as possible to reach error-free transmission ( $\text{BER} < 10^{-12}$ ). When error-free transmission had been reached, the attenuation was increased in steps of 0.5 dB to measure the BER as a function of received optical power. In the following, the results of these transmission experiments are presented. During the measurements, the VCSELs were kept in a room temperature environment.

## 6.1 Back-to-Back

If only a short optical fiber is used between the lens package and the receiver, the quality of the optical signal can be studied without any noticeable influence from dispersion. This is commonly referred to as a back-to-back (BTB) configuration. To ensure that the VCSELs were able to transmit data error-free at the studied data rates, BER measurements were

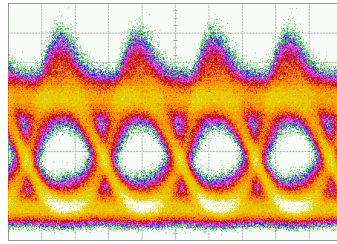


**Figure 6.2:** Eye diagram at 22 Gbit/s for VCSEL A at a bias current of 12 mA, recorded BTB. (30 mV/div, 20 ps/div). The VCSEL did not allow for error-free transmission at this data rate.

performed at every considered data rate. To avoid cluttering of BER plots, lower data rates have been left out since it is obvious that lower data rates than the presented are supported. The BER measurements were performed using different bias currents, but only the bias currents corresponding to the lowest received optical power are included in the plots.

VCSEL A were not able to support error-free transmission at the lowest data rate studied (22 Gbit/s), due to too low damping, but an eye diagram at this data rate can be seen in figure 6.2. In figure 6.3 the BER is plotted as a function of received power at the highest data rates achieved using  $0.99 V_{pp}$  modulation amplitude ( $V_{mod}$ ), which were 45, 54 and 55 Gbit/s for VCSELs B, C and D, respectively. The corresponding eye diagrams can be seen in figures 6.4(c), 6.5(e) and 6.6(e). To be able to compare VCSEL C and D at the same data rate, BER measurements at 50 Gbit/s are also plotted in figure 6.3, while the corresponding eye diagrams can be seen in figures 6.5(d) and 6.6(d). For the same reason, eye diagrams for VCSEL B–D at 22, 40 and 45 Gbit/s are also included in figures 6.4–6.6.

If the recorded eye diagrams are compared, it is obvious that VCSEL A (figure 6.2) has the most overshoot and jitter, due to the low damping. VCSEL B also has quite much overshoot, which seems to give rise to considerable jitter at 45 Gbit/s, see figure 6.4(c). The difference between VCSEL C and D is smaller (figure 6.5 and 6.6), but it is noticeable that VCSEL D has slightly less overshoot and jitter in all eye diagrams, which is a result of the higher damping.

An attempt was also made to increase the maximum data rate for VCSEL C and D through increased modulation amplitude ( $1.35 V_{pp}$ ). This allowed an increase of the data rate for both VCSEL C and D, reaching 56 and 57 Gbit/s, respectively. Plots of the BER measurements can be seen in figures 6.3(b) and (c), while the eye diagrams are presented in figures 6.5(f) and 6.6(f). This is, to the best of the author’s knowledge, the highest serial bit rate ever reported for any VCSEL, both with and without equalization. It should also be noted that the bias current required to obtain 57 Gbit/s with VCSEL D was only 13 mA, compared to the 16 mA required to obtain 56 Gbit/s with VCSEL C. To have a low bias current is of uttermost importance to keep power consumption as low as possible.

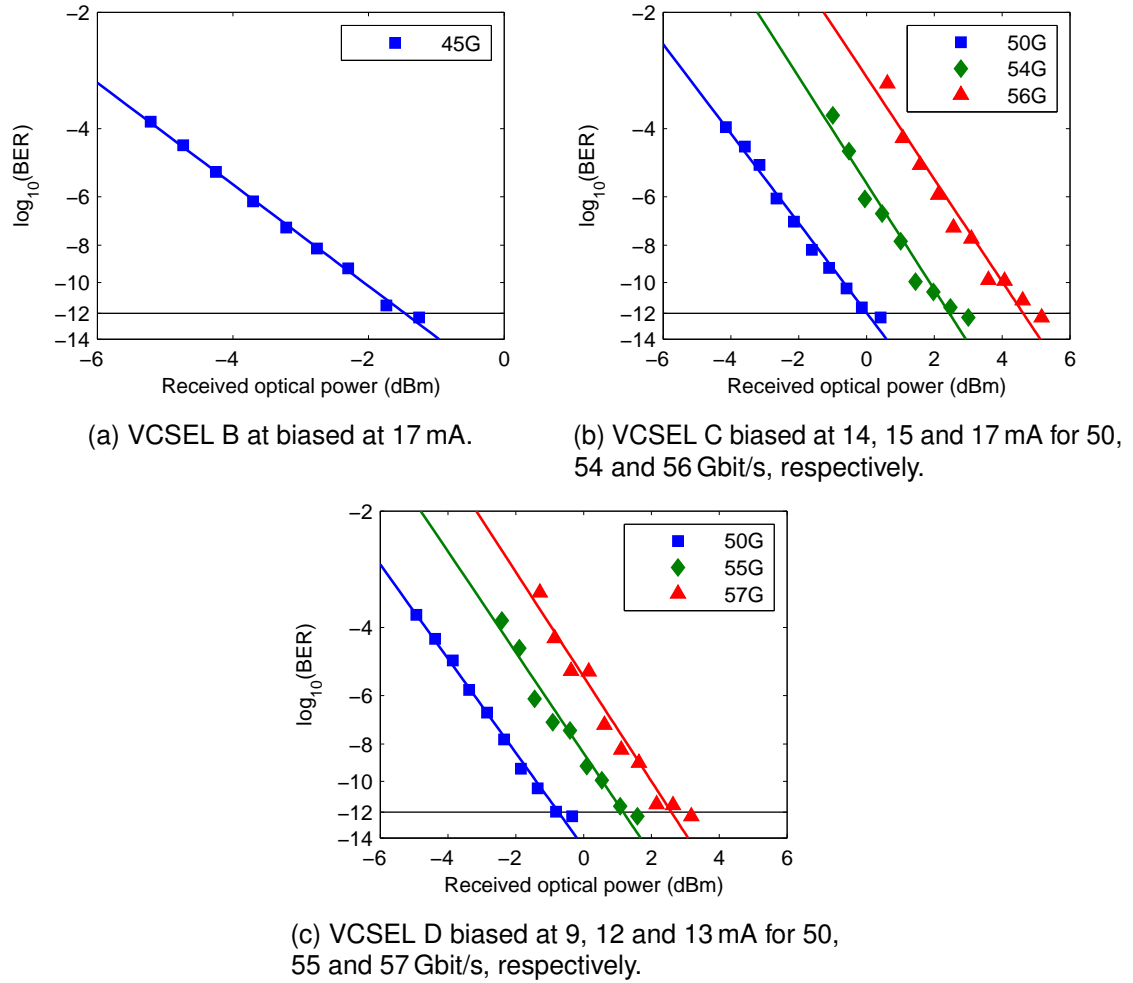


**Figure 6.3:** Bit error rate versus received optical power, measured BTB.

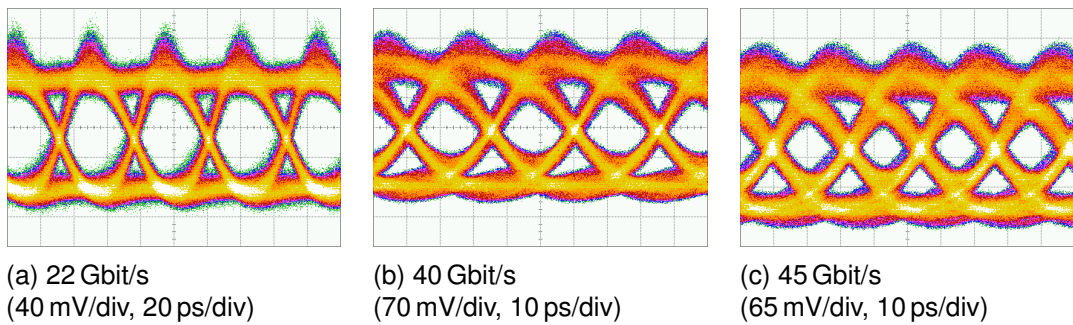


**Figure 6.4:** Eye diagrams for VCSEL B at a bias current of 17 mA, recorded BTB.

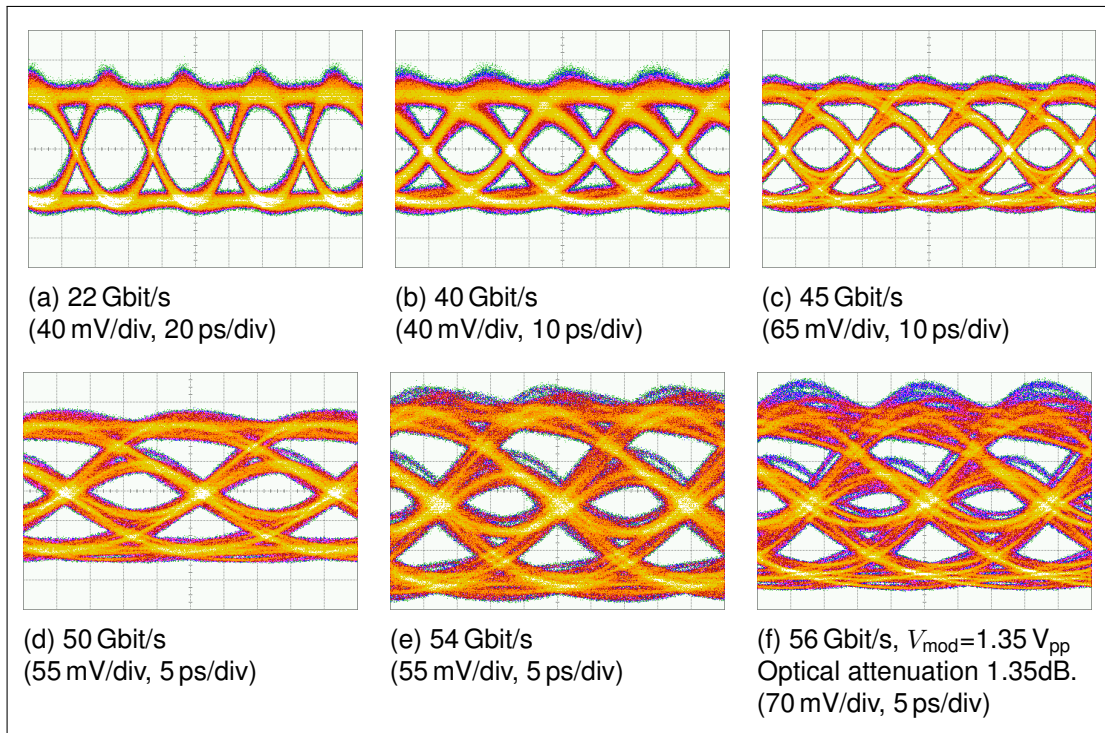


**Figure 6.5:** Eye diagrams for VCSEL C at a bias current of 17 mA, recorded BTB.

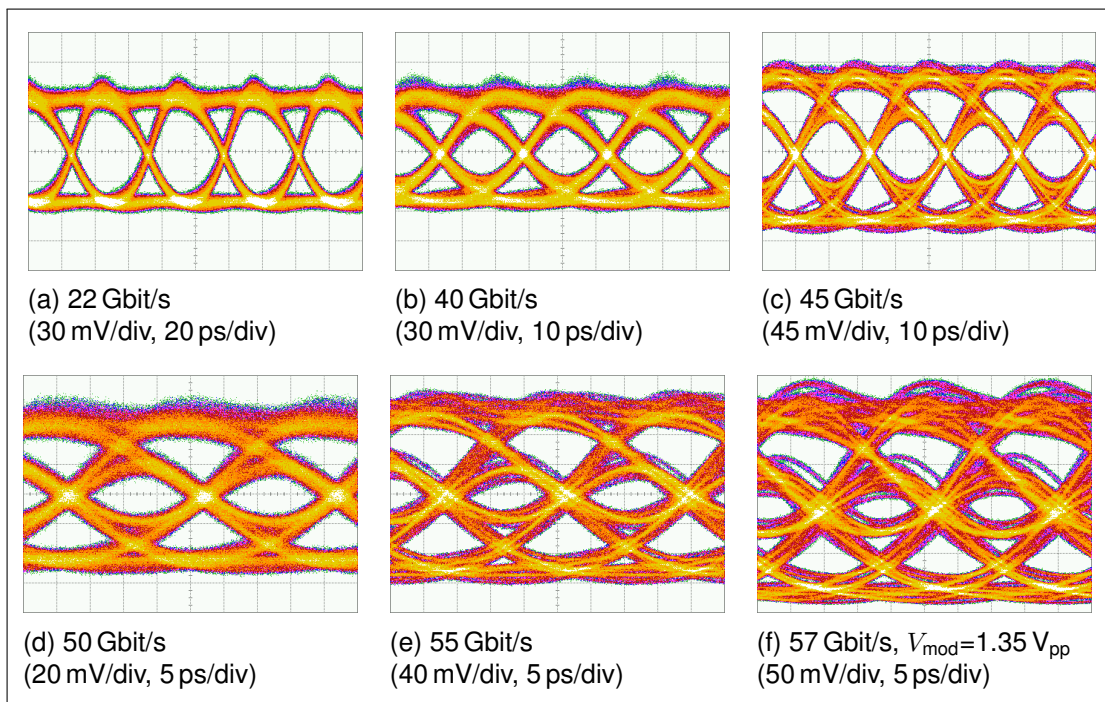


**Figure 6.6:** Eye diagrams for VCSEL D at a bias current of 13 mA, recorded BTB.

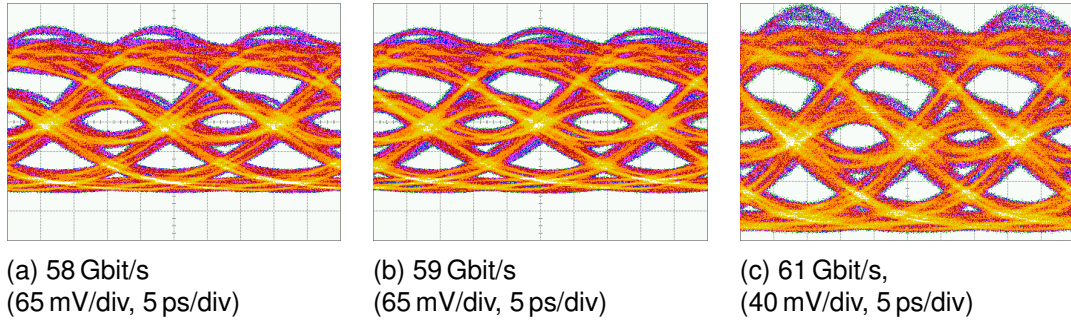


**Figure 6.7:** Eye diagrams above 57 Gbit/s for VCSEL D at a bias current of 13 mA, using  $V_{\text{mod}}=1.35 V_{\text{pp}}$ , recorded BTB. BER could not be measured at these bit rates with the available BERT, since the it did not work above 57 Gbit/s.

The limiting factor for the data rate obtained by VCSEL D seems to be the error analyzer (EA) since it is specified to work with reasonable sensitivity up to 56 Gbit/s, which means that the demands on the incoming signal is rapidly increased at higher bit rates. This is an indication of a really high signal quality from VCSEL D, even at 57 Gbit/s, since it was even possible to obtain error-free transmission above the specified 56 Gbit/s. At 58 Gbit/s, the EA would not even sync using a short coaxial cable (of K-type) directly connected between BPG and EA. The maximum possible data rate for error-free transmission is probably slightly higher than the demonstrated 57 Gbit/s for VCSEL D. Eyes that are somewhat open were achieved at 58, 59 and 61 Gbit/s using this VCSEL, see figure 6.7. Unfortunately something happened to the signal after the amplification at 60 Gbit/s and at bit rates above 61 Gbit/s that led to that the eye diagram of the modulating signal had a spur through its center. These open eyes indicates that error-free operation could probably be possible above the demonstrated 57 Gbits/s if a BERT system supporting higher data rates was available, especially if combined with a faster photoreceiver.

## 6.2 Transmission over Optical Fiber

The effect of transmission over different lengths of fiber was also studied. Since VCSEL D achieved the highest data rate BTB at reasonable bias currents, it was chosen to transmit data over 50 and 100 m optical fiber (of type OM4). The modulation amplitude used was  $1.35 V_{\text{pp}}$ , since it gave the highest possible data rate BTB. The highest bit rates obtained were 55 and 43 Gbit/s over 50 and 100 m, respectively. The bias current used for 55 Gbit/s was 13 mA, while for 43 Gbit/s it was 11 mA. The latter was necessary to keep the spectral width of the modulated light as narrow as possible to reduce the dispersion penalty in the fiber ( $\Delta\lambda_{\text{RMS}} = 1.06 \text{ nm}$  for 13 mA, while for 11 mA  $\Delta\lambda_{\text{RMS}} = 0.93 \text{ nm}$ ). Ideally, the fiber is specified to have 47 GHz bandwidth over 100 m, which almost is fully

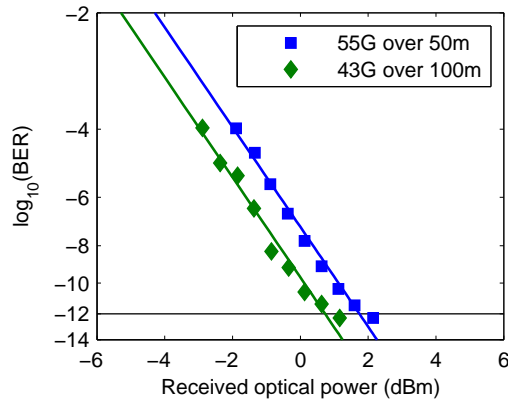


**Figure 6.8:** Bit error rate versus received optical power for VCSEL D biased at 13 and 11 mA, measured after transmission over 50 and 100 m of OM4-fiber, respectively.

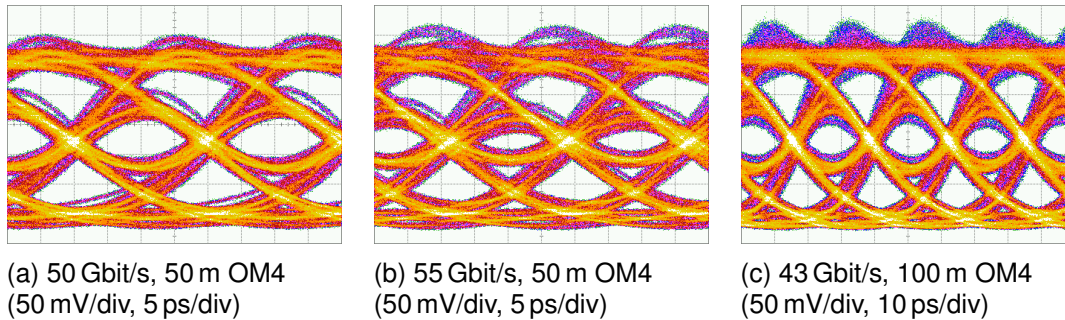


**Figure 6.9:** Eye diagrams for VCSEL D at bias currents of 13 and 11 mA, recorded after transmission over 50 and 100 m of OM4-fiber, respectively, using modulation amplitude  $1.35 V_{pp}$ .

utilized at 43 Gbit/s. The BER at these bit rates and distances of optical fiber is plotted versus received power in figure 6.8, while the eye diagrams can be seen in figure 6.9, where an eye diagram at 50 Gbit/s over 50 m also is included. The bit rates obtained over 50 and 100 m of OM4 fiber is, to the best of the author's knowledge, the highest serial data rate ever reported for any VCSEL over these distances. The demonstration of data transmission with VCSEL D over 50 m of fiber, only slightly below the maximum data rate BTB, is an indication of excellent signal quality.

### 6.3 Back-to-Back Using a Limiting Receiver

The effect of using a limiting receiver was studied by replacing the linear photoreceiver with a VI Systems R40-850 limiting receiver. Using this receiver instead, a bit rate of 49.8 Gbit/s was obtained when VCSEL D was modulated with an amplitude of  $1.35 V_{pp}$ . The BER versus received optical power is plotted in figure 6.10, while the eye diagram

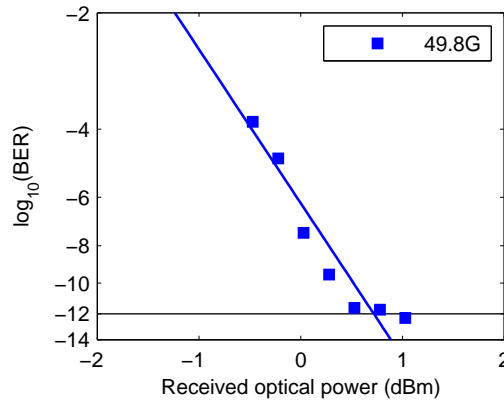


**Figure 6.10:** Bit error rate versus received optical power for VCSEL D biased at 13 mA, measured BTB and using a limiting receiver.

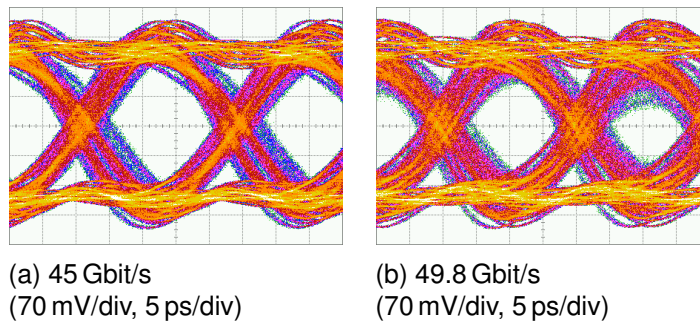


**Figure 6.11:** Eye diagrams for VCSEL D at a bias current of 13 mA, recorded BTB using a limiting receiver with the optical attenuation set to 4 dB and a modulation amplitude of  $1.35 V_{pp}$ .

can be seen in figure 6.11 where an eye diagram at 45 Gbit/s also has been included. Comparing the eye diagrams using the limiting receiver and the linear receiver (figure 6.6), it can clearly be seen that the eye amplitude has increased at the price of introducing more jitter. The introduction of more jitter is a well known effect of using a limiting receiver since it changes amplitude noise into timing jitter, but some of the introduced jitter could also be due to the bandwidth of the receiver. The higher jitter together with the bandwidth of the receiver is likely the reason for the lower data rate obtained with the limiting receiver compared with the linear receiver. The linear receiver has a slow frequency roll off giving a 6 dB bandwidth of 33 GHz, which could explain why it performed better than expected for a 22 GHz receiver.

## Chapter 7

# Measurements of Timing Jitter

The same setup as described for the transmission measurement in chapter 6 was used to measure the jitter of the signal. The measurements were conducted at different bit rates as a function of bias current, while the VCSELs were kept at room temperature. The procedure to measure jitter at each bit rate and bias current were to first find a good sampling point (in time and amplitude) where the error analyzer could sync with the incoming data signal. The equipment's automatic search function was used to find the amplitude offset that should be used during the measurement. The sampling point delay was swept across the transition region (between the bit slots) while the BER was measured during a specified gating time at each delay point, see figure 7.1. Measurements like these are commonly called BERT scans. The variable optical attenuator was set to 3 dB during the measurements.

Unfortunately, the BPG and EA had a multiplexing problem, which led to that the jitter measurements only could be performed at some specific data rates. The bit rates studied were 22, 28, 40 and 45 Gbit/s, where 45 Gbit/s was the highest bit rate at which the jitter measurement worked.

To get reasonable statistical confidence, 10 errors are suggested as a minimum in the Fibre Channel Specification [21]. In the Fibre Channel Specification there are also requirements on the range of BER values used to extrapolate to low BER levels. The maximum BER used should not be higher than  $BER = 1/(10 \cdot \text{pattern length})$ , which for PRBS  $2^7 - 1$  having a pattern length of 127 corresponds to a BER of  $7.9 \cdot 10^{-4}$ . The subsets of BER used should span over at least 3 decades. To fulfill these requirements, BER values between  $10^{-5}$  and  $10^{-10}$  were required in this study. To obtain at least 10 errors at a BER of  $10^{-10}$  a gating time of 4.6, 3.6, 2.5 and 2.3 s was used for 22, 28, 40 and 45 Gbit/s, respectively. To reduce measurement time, the maximum number of errors allowed at each sampling point was set to  $10^5$ .

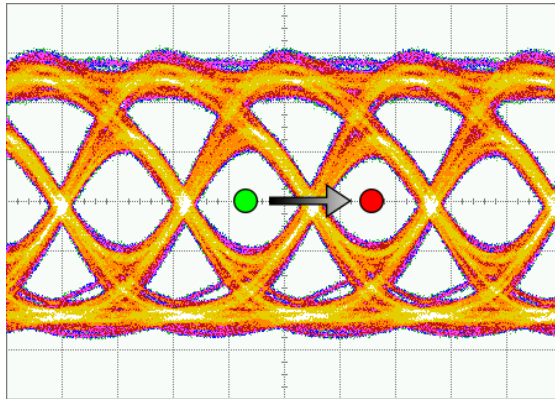
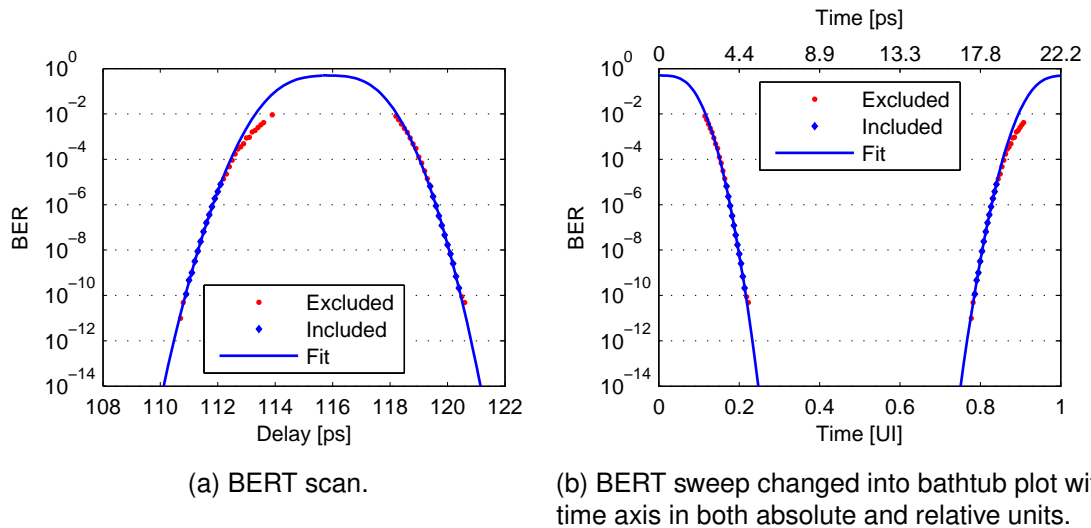


**Figure 7.1:** Eye diagram for VCSEL D at 45 Gbit/s with indications showing how the sampling point is swept across the transition region, from the left green point to the right red point, during a BERT scan.



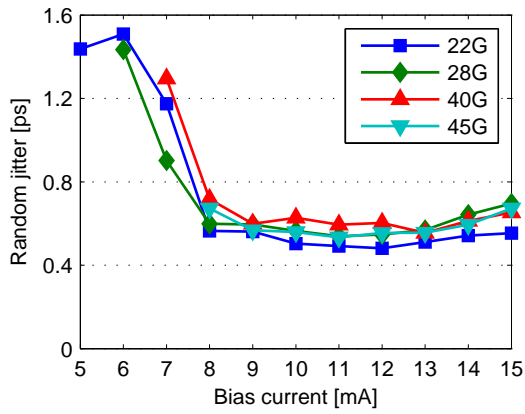
(a) BERT scan.

(b) BERT sweep changed into bathtub plot with time axis in both absolute and relative units.

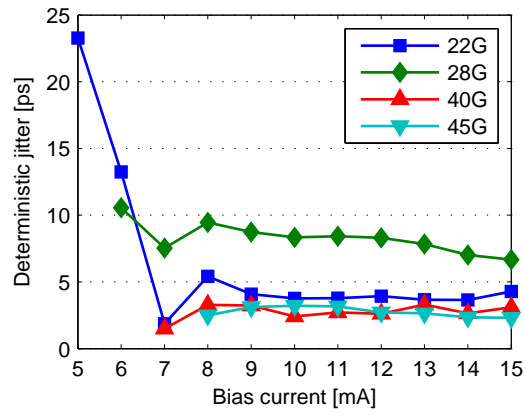
**Figure 7.2:** Jitter measurement, data obtained using VCSEL D at 45 Gbit/s operating at 13 mA bias current and modulation amplitude  $0.99 V_{pp}$ .

**Table 7.1:** The jitter of the measurement system

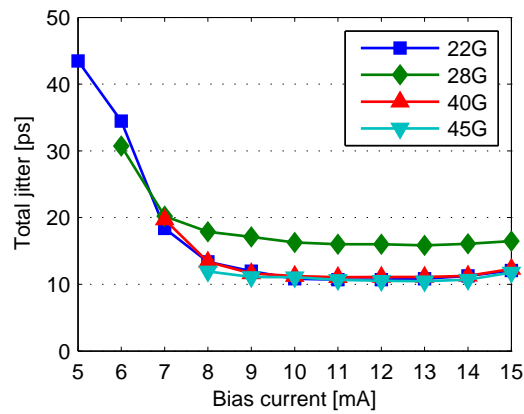
$B$ [Gbit/s]	RJ [ps]	DJ [ps]	TJ [ps (UI)]
22	0.24	3.5	6.9 (0.15)
28	0.34	5.0	9.7 (0.27)
40	0.11	3.7	5.2 (0.21)
45	0.096	2.7	4.0 (0.18)



(a) Random jitter.



(b) Deterministic jitter.



(c) Total jitter.

**Figure 7.3:** Extracted values from jitter measurements BTB for VCSEL D using  $V_{\text{mod}} = 0.99 V_{\text{pp}}$ .

The acquired data with BER between  $10^{-5}$  and  $10^{-10}$  was then fitted to the dual-Dirac model in (4.15) and (4.16) to extract the jitter parameters random jitter, deterministic jitter and total jitter. A typical measurement with fit looks like the one in figure 7.2(a) obtained for VCSEL D biased at 13mA and operating at 45 Gbit/s. This kind of measurement can be rearranged into a so called bathtub plot, which is a more commonly used visualization. The technique has been used for the measurement in figure 7.2(a) and the result can be seen in figure 7.2(b) with time axis in both absolute and relative units.

BERT scans were performed at different data rates and bias points and the result for VCSEL D using BTB configuration can be seen in figure 7.3, while the corresponding results for VCSEL B and C can be found in appendix C. It can be seen that the jitter looks very similar at all bit rates except for 28 Gbit/s, which is due to larger jitter in the signal from the measurement system at this particular bit rate. To study the modulation signal used, the jitter was also measured without the laser, but including amplifier, bias-T and cables. The extracted jitter parameters for the measurement system can be found in table 7.1. In the following, results for the VCSELs are plotted for the same bit rate in the same figures for easier comparison.

## 7.1 Back-to-Back

The jitter was measured back-to-back using VCSELs B–D and the results at 45 Gbit/s are plotted in figure 7.4. VCSEL A was excluded from this investigation because error-free transmission was not possible. VCSEL B has the highest TJ, due to having both the highest RJ and the highest DJ. In the figure, it can also be seen that the lowest total jitter was obtained with VCSEL C. From the extracted jitter parameters in figure 7.4(a) and (b) it can be seen that VCSEL D has lower deterministic jitter and higher random jitter than VCSEL C. Since the total jitter is a sum of the deterministic jitter and roughly 14 times the random jitter, this is the reason the total jitter was higher with VCSEL D than with VCSEL C. The reason of VCSEL D having higher random jitter is possibly that the maximum output power is lower, which could result in lower signal-to-noise-ratio (SNR) which affects RJ.

The amount of damping affects the amount of inter symbol interference, which is a data dependent deterministic jitter component. The ISI is caused by limitations set by the frequency response, both through bandwidth and damping. The amount of damping in the laser will affect both the bandwidth and the overshoot of the data transitions, which means that there is a trade-off between high bandwidth and low overshoot. The bandwidth limitations will shrink the eye opening during fast transitions (e.g. 101010), while overshoot due to relaxation oscillations will occur during slower transitions (e.g. 000111). This will introduce ISI since the timing of the transitions between ones and zeros depends on the rise and fall times which in turn depend on the data sequence. A study of the influence of damping on jitter therefore requires DJ and RJ to be analyzed separately. The damping affects DJ directly, while RJ is indirectly affected since the

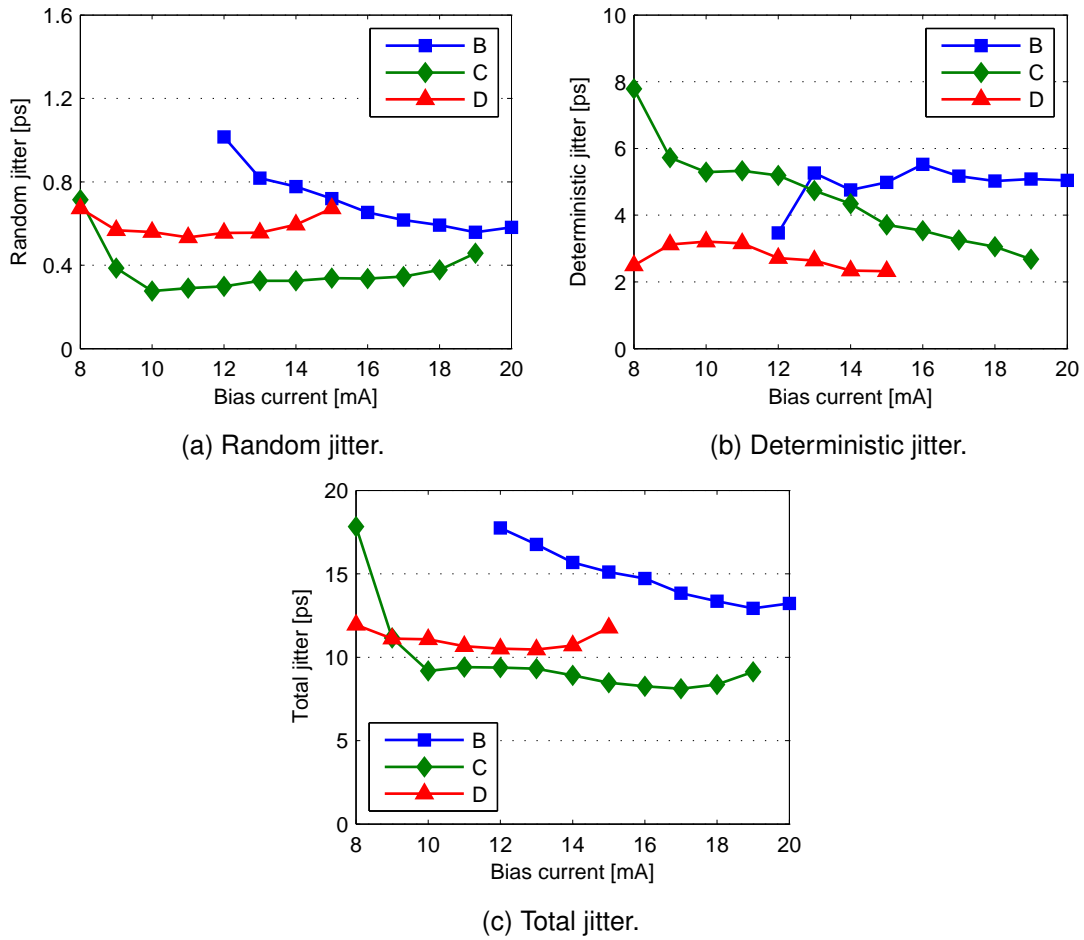


**Figure 7.4:** Extracted values from jitter measurements BTB at 45 Gbit/s using  $V_{\text{mod}} = 0.99 V_{\text{pp}}$ .

optical output power, which affects the obtained SNR, depend indirectly on the amount of damping in the VCSEL. The output power can be assumed to be the same when the bit rate is increased, however, the amount of ISI introduced is highly dependent on the data rate.

The DJ at 45 Gbit/s is highest for VCSEL B, and higher for VCSEL C than for VCSEL D, see figure 7.4(b). This is due to that VCSEL B has the lowest damping, while the damping of VCSEL C is lower than that of VCSEL D. Lower damping will introduce more ISI due to overshoot and relaxation oscillations. Since VCSEL C has a higher output power than VCSEL D, the height of the whole eye will be larger, which will increase the SNR and therefore introduce a lower RJ. Since the VCSELs are not limited by DJ due to ISI at these data rates, the SNR will be limiting the total jitter.

However, at higher bit rates when the ISI is more pronounced and limiting the total jitter, it is most likely that the total jitter of VCSEL D is lower than that of VCSEL C. This would make lower DJ due to higher damping in VCSEL D a likely explanation why VCSEL D was able to transmit data at a higher data rate than VCSEL C, see chapter 6.

## 7.2 Impact of Using Higher Modulation Amplitude

Since error-free transmission was made possible at higher data rates when using higher modulation amplitude, an investigation of its impact on jitter was made at 45 Gbit/s. The result can be seen in figure 7.5. Using the higher modulation amplitude ( $1.35 V_{pp}$  instead of  $0.99 V_{pp}$ ), the total jitter is improved for VCSEL D. This is due to that the random jitter has been decreased with more than a factor of two, while the deterministic jitter only has increased slightly. The lower random jitter indicates a higher SNR, while the increased deterministic jitter indicates a reduced bandwidth. VCSEL C, however, seem to obtain worse jitter performance using the higher modulation amplitude, mostly due to that the deterministic jitter has been increased, while the random jitter only is slightly decreased. This indicates that the SNR is only increased by a negligible amount while the bandwidth is sacrificed nevertheless.

The reason why VCSEL D gained from increasing the modulation amplitude is probably due to that the signal amplitude, and therefore SNR, is increased by the higher modulation amplitude. The higher modulation amplitude increases the amount of overshoot and excessive relaxation oscillations, but the high damping in the modulation response of VCSEL D seems to be high enough to avoid too much of these effects. VCSEL C, however, has slightly less damping and seems to suffer from more overshoot and relaxation oscillations when the modulation amplitude is increased. The modulation amplitude used seems to set a requirement on the strength of the damping needed to avoid introducing too much jitter due to overshoot and relaxation oscillations. As long as the modulation amplitude can be increased without affecting the overshoot and relaxation oscillations notably, the corresponding increase of SNR will lead to lower total jitter due to decreased random jitter, as in the case of VCSEL D.

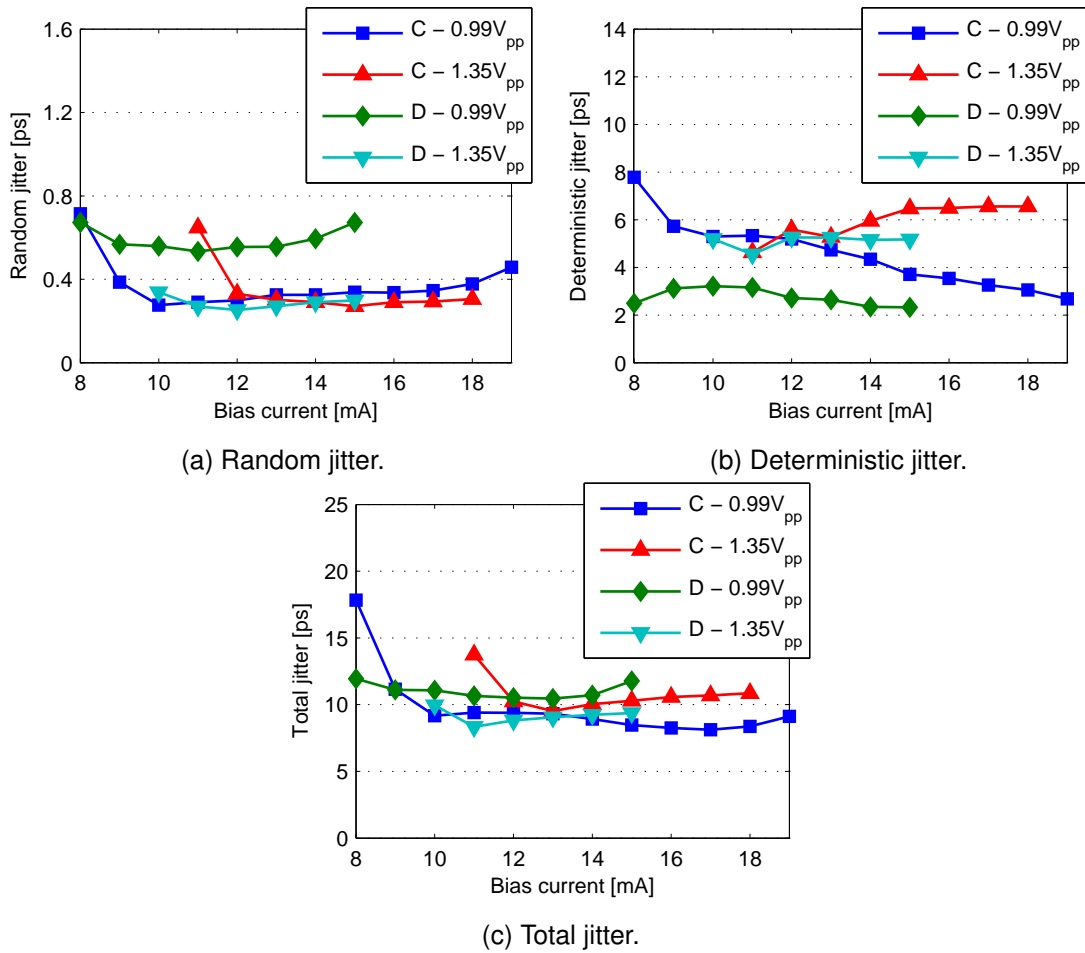


**Figure 7.5:** Extracted values from jitter measurements BTB at 45 Gbit/s using  $V_{\text{mod}} = 0.99 V_{\text{pp}}$  and  $V_{\text{mod}} = 1.35 V_{\text{pp}}$ .

Since VCSEL C does not gain from increasing the modulation amplitude, it is interesting to compare VCSEL D using  $V_{\text{mod}} = 1.35 V_{\text{pp}}$  with VCSEL C using  $V_{\text{mod}} = 0.99 V_{\text{pp}}$ . In figure 7.5(c) it can be seen that the total jitter is lower for VCSEL D than VCSEL C at low bias currents (around 11 mA), while the jitter is at comparable levels for VCSEL C at higher bias currents, above the thermal rollover of VCSEL D.

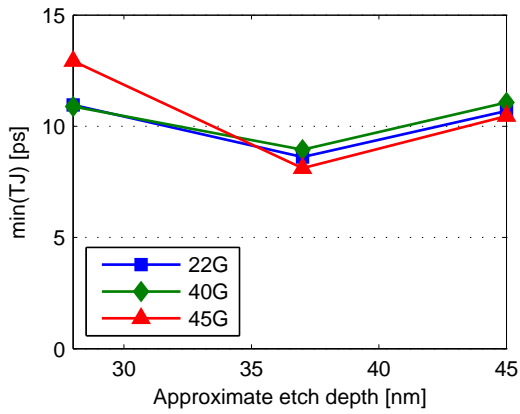
### 7.3 Comparison of Jitter Performance

To simplify the comparison between the VCSELs, the minimum obtained total jitter at different bit rates is plotted versus both etch depth and bit rate in figures 7.6(a) and (b). The result for VCSEL D using modulation amplitude  $1.35 V_{\text{pp}}$  is also included in the figure due to the increased performance associated with the higher modulation amplitude for this component. Note that the modulation signal from the BPG at 28 Gbit/s has much higher jitter than the rest, see table 7.1, and the data rate has therefore been excluded from the plots. The modulation signals at the other data rates have slightly different jitter performance as well. They are therefore a bit hard to compare. However, the lasers can still be compared at the same bit rate, with good confidence.

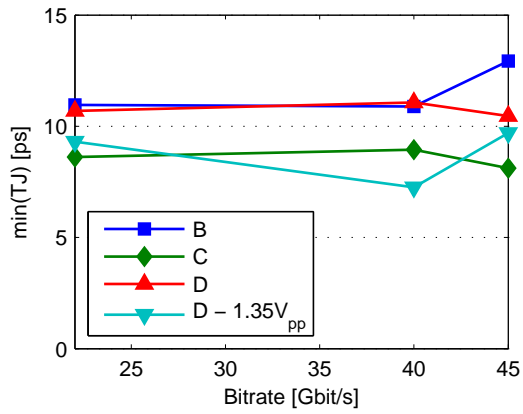
In figure 7.6(d) the deterministic jitter which gave the lowest total jitter has been plotted versus etch depth. The DJ is almost constant for 22 and 40 Gbit/s, but when the bit rate is increased to 45 Gbit/s it is obvious that the induced deterministic jitter is dependent on etch depth, and therefore damping. The random jitter in figure 7.6(c) is, however, almost constant for the different data rates, while the random jitter seems to have some dependence on the etch depth, which is more evident in figure 7.4(a).

The dependence between total jitter and etch depth in figure 7.6(a) can be explained by that TJ is first decreased due to the increased bandwidth and therefore decreased DJ, when the VCSEL is etched. For a deeper etch the total jitter is increased again due to the increased photon lifetime which is inducing lower output power and therefore smaller eye amplitude. However, the deepest etch depth studied still obtains better DJ due to the better high-speed properties induced by the higher damping, i.e. suppression of relaxation oscillations, which indicates why VCSEL D has the best high-speed performance. It is probable that an even higher damped VCSEL would have increased DJ and decreased output power, due to the decreased bandwidth and outcoupling of light. That would lead to worse high-speed large signal properties, which means that there exists an optimum damping, probably close to that of VCSEL D.

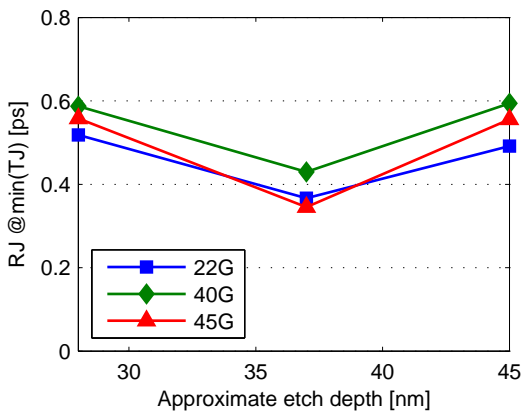
Apart from the result at 28 Gbit/s, the total jitter is almost constant, and the deviations are probably within the measurement accuracy. It could be assumed that the total jitter is independent of the bit rate, but that assumption relies on that the deterministic jitter does not increase much when the bit rate increases. This is not true in reality, since the deterministic component has some bit rate dependence, as seen in figure 7.6(d). However, the assumption that the total jitter is constant would allow for a prediction of



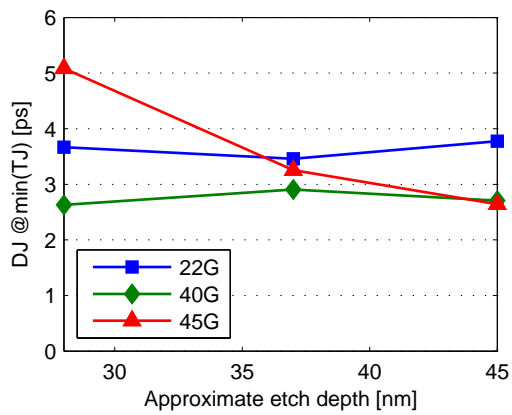
(a) Minimum total jitter vs. etch depth.



(b) Minimum total jitter vs. data rate.



(c) Random jitter giving minimum total jitter.



(d) Deterministic jitter giving minimum total jitter.

**Figure 7.6:** Minimum total jitter and corresponding jitter parameters extracted from the measurements BTB.

the maximum possible jitter limited bit rate, if there is knowledge of how much jitter the system can handle. The specification given, in the jitter part of the Fiber Channel standard [21], is 0.52 UI. Assuming that total jitter performance should be at this limit and that the total jitter is not increased with the data rate, the values in figure 7.6 can be used to predict the maximum possible jitter limited error-free data rate. In the figure, the minimum total jitter at 45 Gbit/s is roughly 8 ps for both VCSEL C and D which corresponds to 0.52 UI at 65 Gbit/s. At this high data rate other factors will also contribute and limit the possible bit rate. This can clearly be seen by studying the eye diagrams above 50 Gbit/s, in figures 6.5–6.7 where the eye diagrams are starting to close vertically and thereby probably are more limited by the vertical eye opening than the introduced jitter. However, the eye obtained at 61 Gbit/s (figure 6.7(c)) is at least somewhat open, and not that far from the predicted 65 Gbit/s.

## 7.4 Transmission over Optical Fiber

Since VCSEL D was able to transmit error-free at the highest bit rate it was also evaluated through fiber optical transmission over 50 and 100 m of OM4-fiber. The result of the jitter measurement at 40 Gbit/s is plotted in figure 7.7. As expected, the total jitter increases with increased length of fiber. It is interesting to see though, that 50 m of OM4-fiber only increases the total jitter marginally, which probably is the reason that 55 Gbit/s was possible to obtain over this distance. Over 100 m of fiber, however, the total jitter has increased with more than 50% compared with over 50 m, which is due to inter symbol interference introduced by dispersion, since the  $\Delta\lambda_{\text{RMS}}$  is larger than what OM4 is specified for. The dispersion also manifested itself while measuring the BER (see section 6.2) by the need of using a lower bias current, corresponding to smaller spectral width, to avoid too much inter symbol interference and achieve error-free transmission at 43 Gbit/s over 100 m.

It seems like the random jitter is most affected by the fiber transmission, especially over 100 m. This is a bit surprising since jitter induced by dispersion, i.e. ISI, has deterministic behavior (see section 4.3). It is probable that the reason for this is that the dispersion is introducing a penalty on the SNR, i.e. the received power is required to be higher to obtain error-free transmission, which means that the jitter measurement (at 3 dB optical attenuation) is performed closer to the error-free limit and will therefore be more influenced by noise which will introduce more random jitter. However, this could also be a result of the physical incorrectness of the dual-Dirac model, as discussed in section 4.4.1.

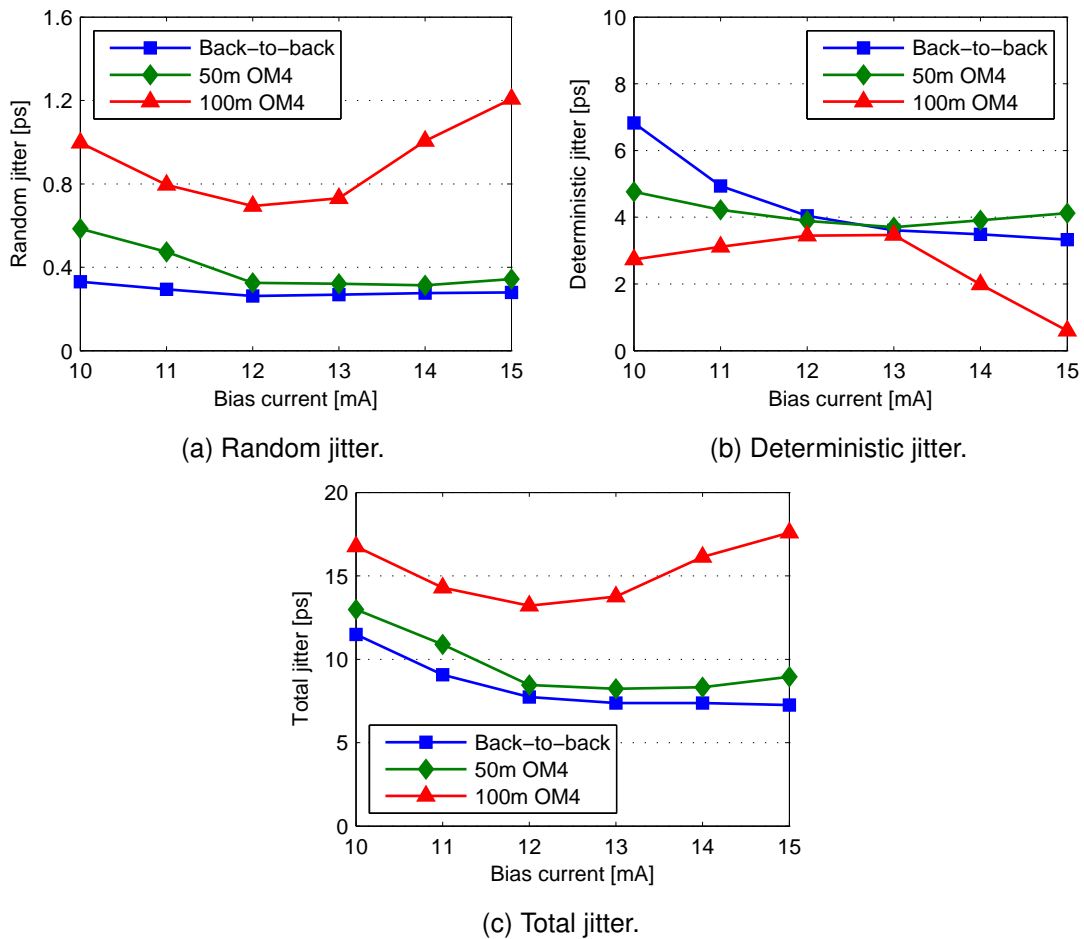
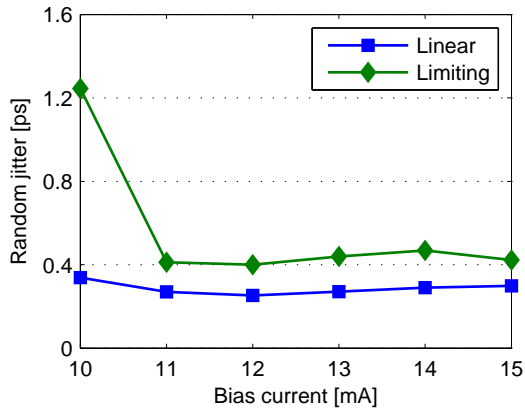


**Figure 7.7:** Extracted values from jitter measurements at 40 Gbit/s over fibers of different lengths using modulation amplitude  $1.35 V_{pp}$ .

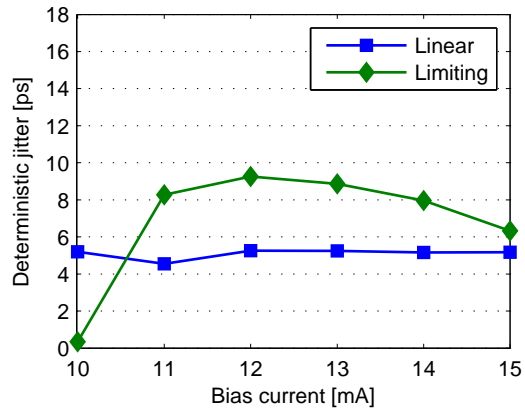
## 7.5 Impact of Using a Limiting Receiver

VCSEL D was also evaluated using a limiting receiver instead of the usual linear receiver. The measured jitter is plotted in figure 7.8, where it is clear that the total jitter is much higher for the limiting receiver. The obtained result is expected since a limiting receiver will change noise and eye closure into jitter, which easily can be seen by comparing the eye diagrams obtained using a linear receiver, in figure 6.6, with the ones obtained using a limiting receiver, in figure 6.11, where eye closure obviously has been opened a bit at the price of introducing more jitter. The increase of total jitter is mostly due to increased DJ, which probably is a result of that the receiver's bandwidth limitation is causing ISI and that amplitude noise is transformed into duty cycle distortion in a limiting receiver. The random jitter is still quite low, which indicates that the SNR is good, but since a limiting receiver should increase the SNR to the price of introducing more jitter, the RJ is expected to decrease instead. This means that the performance, at very high data rates, of the VI Systems limiting receiver is not as good as that of the New Focus linear receiver. However, at more moderate data rates the limiting receiver will obtain higher SNR and well defined signal levels, which is important for implementation in commercial systems.

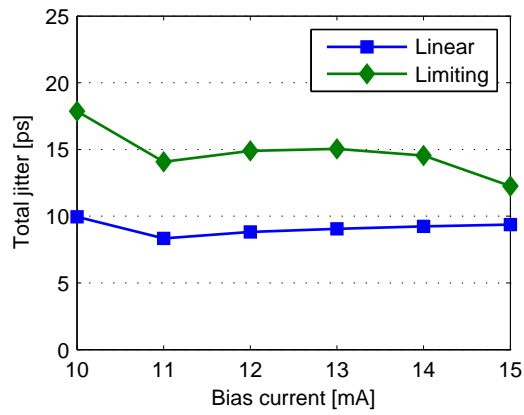
Using the same prediction technique as in Section 7.3 the minimum total jitter of about 12 ps corresponds to 0.52 UI at a bit rate of 43 Gbit/s. At 49.8 Gbit/s, the maximum error-free data rate obtained with the limiting receiver, 12 ps corresponds to 0.60 UI. This could probably explain why the linear receiver is capable of receiving higher data rates. The result makes it clear that the data transmission is limited by the receivers. The VCSELs, and especially VCSEL D, have high-speed properties which probably could support even higher bit rates. Perhaps this could be obtained using a linear receiver with higher bandwidth than the 22 GHz linear photoreceiver used.



(a) Random jitter.



(b) Deterministic jitter.



(c) Total jitter.

**Figure 7.8:** Extracted values from jitter measurements, at 45 Gbit/s with linear and limiting receiver using modulation amplitude  $1.35 V_{pp}$ .



## Chapter 8

# Conclusion

This project has studied the influence of the damping on the VCSEL's ability to transmit high-speed data. Four VCSELs (A–D) with different degrees of damping were investigated and static and dynamic properties were characterized. VCSEL C showed the highest small signal bandwidth (25.0 GHz), while the highest bit rate was obtained with VCSEL D. The highest data rates obtained were 57 Gbit/s back-to-back, 55 Gbit/s over 50 m of OM4-fiber and 43 Gbit/s over 100 m of OM4-fiber, all obtained by VCSEL D biased at 13 mA or less and all record high bit rates for directly modulated VCSELs using on-off keying.

The damping's effect on the timing jitter was also studied and it was concluded that the total jitter (measured in absolute units) seems to be independent of the data rate, at least up to 45 Gbit/s. The timing jitter is, however, dependent on the damping of the laser. This is due to the deterministic jitter component which is highly dependent on the damping and to some extent also on the data rate. A VCSEL with higher damping will introduce less deterministic jitter than a VCSEL with lower damping by reducing the overshoot and the relaxation oscillations. However, too much damping will eventually limit both the bandwidth and the SNR through an associated reduction in output power. The total jitter was lower for VCSEL C than VCSEL D which, however, had lower deterministic jitter than VCSEL C using  $0.99 V_{pp}$  modulation amplitude. Using a higher modulation amplitude ( $1.35 V_{pp}$ ), the total jitter was decreased for VCSEL D while it was increased for VCSEL C. This indicates that higher damping is beneficial when an increased signal amplitude is used to increase the SNR, probably due to that overshoot and relaxation oscillations still can be sufficiently damped. Using the obtained jitter at 45 Gbit/s, it is predicted that the jitter limited data rate is 65 Gbit/s. However, the eyes obtained at 57 Gbit/s using VCSEL D are already more limited by the amplitude of the eye opening than by the jitter, which indicates that the bandwidth of the whole system is limiting the data rate.

The total bandwidth of the system is a combination of the bandwidths of all parts in the system and the receiver seemed to be the limiting part in the setup. Indications supporting this were seen during the brief investigation of using a limiting photoreceiver instead of a linear one. The limiting photoreceiver, specified to 30 GHz, could only handle 49.8 Gbit/s compared to the 57 Gbit/s for the linear 22 GHz receiver, whose frequency response, however, has a rather slow roll off (33 GHz 6 dB bandwidth).

The timing jitter introduced after propagation over 50 and 100 m of OM4-fiber was also studied. It was clear that the jitter is almost unaffected after 50 m, but largely affected after 100 m, which means that the observed jitter at 100 m is due to dispersion. However, the measured jitter distribution indicated an increase of random jitter, which could be due to a SNR penalty induced by dispersion, but could also be caused by the physical incorrectness of the dual-Dirac model.

The receiver's influence on the signal needs further understanding, and hopefully better receivers are developed, in research and industry, which could be used to test the VCSELs at even higher bit rates. That also means that a BERT operating at higher data rates than 56 Gbit/s are needed. Further, a deeper study on the dependence of jitter induced by dispersion would be interesting, i.e. the influence of fiber length together with the VCSEL's properties (i.e. spectral width, damping, bandwidth etcetera). Finally the influence of damping on the VCSELs' high-speed large signal properties also needs further study. Its effect on the rise and fall times, SNR and eye opening is not yet completely understood.

# Bibliography

- [1] C. Kachris and I. Tomkos, “A survey on optical interconnects for data centers,” *Communications Surveys Tutorials, IEEE*, vol. 14, no. 4, pp. 1021–1036, 2012.
- [2] A. Kasukawa, K. Takaki, S. Imai, H. Shimizu, Y. Kawakita, K. Hiraiwa, M. Funabashi, T. Suzuki, N. Tsukiji, S. Kamiya, and T. Ishikawa, “Enabling VCSEL technology for ‘green’ optical interconnect in HPC and data centers,” in *Photonics Conference (PHO), 2011 IEEE*, Oct. 2011, pp. 393–394.
- [3] K. Schmidtke and F. Flens, “Trends and future directions in optical interconnects for datacenter and computer applications,” in *Optical Fiber Communication (OFC), collocated National Fiber Optic Engineers Conference, 2010 Conference on (OFC/NFOEC)*, march 2010, pp. 1–3.
- [4] R. Ho, J. Cunningham, H. Schwetman, X. Zheng, and A. Krishnamoorthy, “Optical interconnects in the data center,” in *High Performance Interconnects (HOTI), 2010 IEEE 18th Annual Symposium on*, Aug. 2010, pp. 117–120.
- [5] A. Vahdat, H. Liu, X. Zhao, and C. Johnson, “The emerging optical data center,” in *Optical Fiber Communication Conference and Exposition (OFC/NFOEC), 2011 and the National Fiber Optic Engineers Conference*, Mar. 2011, pp. 1–3.
- [6] P. Pepeljugoski, F. Doany, D. Kuchta, L. Schares, C. Schow, M. Ritter, and J. Kash, “Data center and high performance computing interconnects for 100 Gb/s and beyond,” in *Optical Fiber Communication and the National Fiber Optic Engineers Conference, 2007. OFC/NFOEC 2007. Conference on*, 2007, pp. 1–3.
- [7] D. Dolfi, “Multi-channel optical interconnects for short-reach applications,” in *Electronic Components and Technology Conference, 2003. Proceedings. 53rd*, 2003, pp. 1032–1039.
- [8] A. Larsson, “Advances in VCSELs for communication and sensing,” *Selected Topics in Quantum Electronics, IEEE Journal of*, vol. 17, no. 6, pp. 1552–1567, Nov.–Dec. 2011.
- [9] A. Larsson, J. Gustavsson, Å. Haglund, J. Bengtsson, B. Kögel, P. Westbergh, R. Safaisini, E. Haglund, K. Szczerba, M. Karlsson, and P. Andrekson, “High speed

- VCSELs for optical interconnects,” in *Indium Phosphide and Related Materials (IPRM), 2012 International Conference on*, Aug. 2012, pp. 269–272.
- [10] P. Westbergh, J. Gustavsson, B. Kögel, Å. Haglund, A. Larsson, and A. Joel, “Speed enhancement of VCSELs by photon lifetime reduction,” *Electronics Letters*, vol. 46, no. 13, pp. 938–940, Jun. 2010.
- [11] P. Westbergh, J. Gustavsson, B. Kögel, Å. Haglund, and A. Larsson, “Impact of photon lifetime on high-speed VCSEL performance,” *Selected Topics in Quantum Electronics, IEEE Journal of*, vol. 17, no. 6, pp. 1603–1613, Nov.–Dec. 2011.
- [12] P. Westbergh, R. Safaisini, E. Haglund, J. Gustavsson, A. Larsson, M. Geen, R. Lawrence, and A. Joel, “High-speed oxide confined 850-nm VCSELs operating error-free at 40 Gb/s up to 85°C,” *Photonics Technology Letters, IEEE*, vol. 25, no. 8, pp. 768–771, 2013.
- [13] D. Kuchta, A. Rylyakov, C. Schow, J. Proesel, F. Doany, C. W. Baks, B. Hamel-Bissell, C. Kocot, L. Graham, R. Johnson, G. Landry, E. Shaw, A. MacInnes, and J. Tatum, “A 56.1Gb/s NRZ modulated 850nm VCSEL-based optical link,” in *Optical Fiber Communication Conference/National Fiber Optic Engineers Conference 2013*. Optical Society of America, 2013, p. OW1B.5.
- [14] Acquire Media, “Oclaro samples 20G VCSEL; extends VCSEL leadership by shipping more than 500k 10G VCSELs,” Jan. 2012, accessed 15 Jan. 2013. [Online]. Available: <http://investor.oclaro.com/releasedetail.cfm?releaseid=641498>
- [15] T. H. Maiman, “Stimulated optical radiation in ruby,” *Nature*, vol. 187, no. 4736, pp. 493–494, 1960.
- [16] A. Larsson, *Semiconductor Optoelectronics - Device Physics and Technologies*. Chalmers University of Technology, 2011.
- [17] L. Coldren and S. Corzine, *Diode Lasers and Photonic Integrated Circuits*. John Wiley & Sons, Inc., 1995.
- [18] P. Westbergh, “High speed vertical cavity surface emitting lasers for short reach communication,” Ph.D. dissertation, Photonics Laboratory, Department of Microtechnology and Nanoscience (MC2), Chalmers University of Technology, Göteborg, April 2011.
- [19] E. Haglund, A. Haglund, P. Westbergh, J. S. Gustavsson, B. Kögel, and A. Larsson, “25 Gbit/s transmission over 500 m multimode fibre using 850 nm VCSEL with integrated mode filter,” *Electronics Letters*, vol. 48, no. 9, pp. 517–519, 2012.
- [20] J. Redd, “Calculating statistical confidence levels for error-probability estimates,” *Lightwave Magazine*, vol. 21, no. 5, pp. 110–114, Apr. 2000.
- [21] B. Ham, “Fibre Channel – Methodologies for jitter and signal quality specification -

- 
- MJSQ,” International Committee for Information Technology Standards (INCITS), Tech. Rep., June 2004.
- [22] D. Wallace and R. Johnson, “Fibre Channel – Methodologies for signal quality specification - MSQS,” International Committee for Information Technology Standards (INCITS), Tech. Rep., Sept. 2010.
- [23] J. Hancock, “Jitter – Understanding it, measuring it, eliminating it; Part 1: Jitter fundamentals,” *High Frequency Electronics*, pp. 44–50, April 2004.
- [24] J. Hancock, “Jitter – Understanding it, measuring it, eliminating it; Part 3: Causes of jitter,” *High Frequency Electronics*, pp. 28–34, June 2004.
- [25] M. Kossel and M. Schmatz, “Jitter measurements of high-speed serial links,” *Design Test of Computers, IEEE*, vol. 21, no. 6, pp. 536–543, 2004.
- [26] M. Li, J. Wilstrup, R. Jessen, and D. Petrich, “A new method for jitter decomposition through its distribution tail fitting,” in *Test Conference, 1999. Proceedings. International*, 1999, pp. 788–794.
- [27] D. J. Law and W. W. Diab, “IEEE standard for ethernet,” IEEE Computer Society, Tech. Rep., Dec. 2012.
- [28] M. Li and J. Chen, “New methods for receiver internal jitter measurement,” in *Test Conference, 2007. ITC 2007. IEEE International*, 2007, pp. 1–10.
- [29] *Application Note AN-JITTER-1: Jitter Analysis using SHF 10000 Series Bit Error Rate Testers*, SHF Communication Technologies AG, Dec. 2005.
- [30] L. Råde and B. Westergren, *Mathematics Handbook for Science and Engineering*. Studentlitteratur, 2003.
- [31] M. Li and J. Wilstrup, “On the accuracy of jitter separation from bit error rate function,” in *Test Conference, 2002. Proceedings. International*, 2002, pp. 710–716.
- [32] T. Yamaguchi, K. Ichiyama, H. Hou, and M. Ishida, “A robust method for identifying a deterministic jitter model in a total jitter distribution,” in *Test Conference, 2009. ITC 2009. International*, 2009, pp. 1–10.
- [33] M. Aleksic, “Extraction of jitter parameters from ber measurements,” in *Electrical Performance of Electronic Packaging and Systems (EPEPS), 2011 IEEE 20th Conference on*, 2011, pp. 63–66.
- [34] R. Stephens, “Jitter analysis: The dual-Dirac model, RJ/DJ, and Q-scale,” Agilent Technologies, White paper, Dec. 2004.



## Appendix A

# Small Signal Modulation Response

In this appendix the additional modulation responses have been plotted in figure A.1.

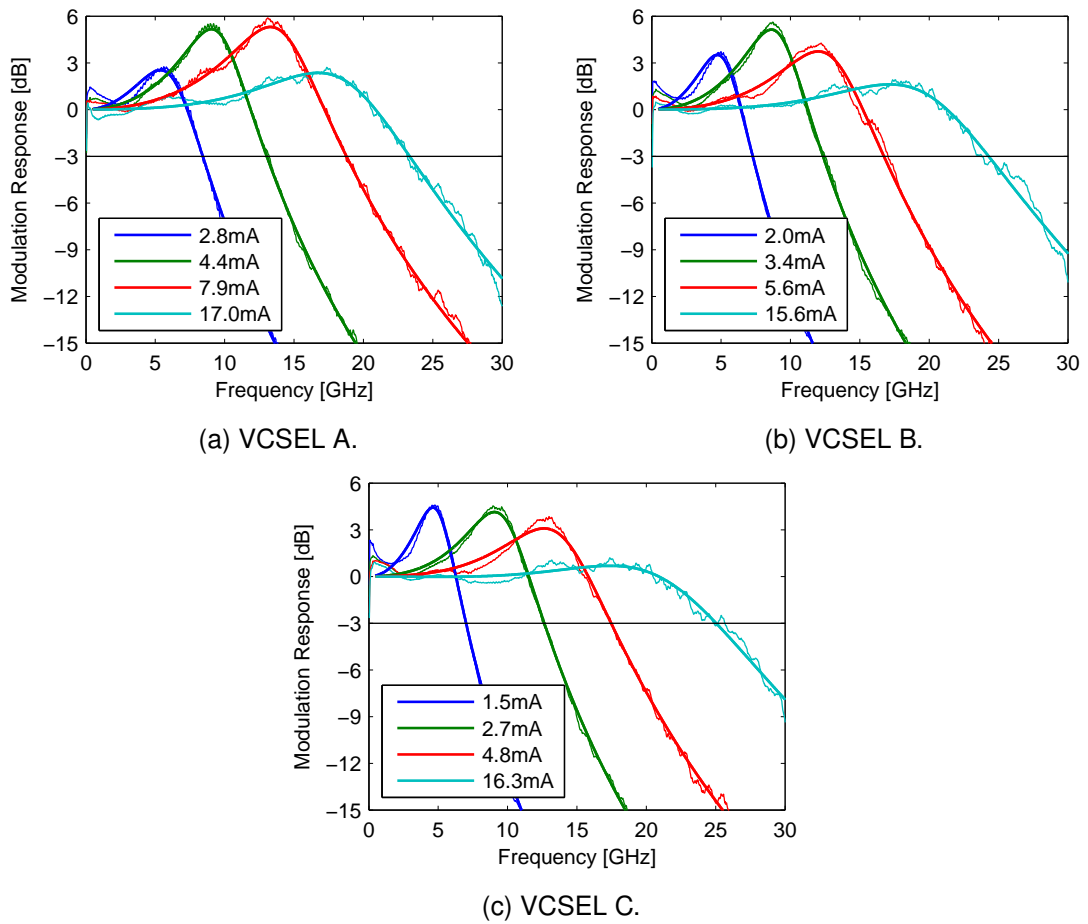


**Figure A.1:** Small signal modulation response of VCSEL A–C for different bias currents. The responses at the largest bias current indicated correspond to the responses with the laser specific maximum 3 dB bandwidths.

## Appendix B

# Eye Diagrams of the Modulation Signal

In this appendix eye diagrams of the data signal, obtained after the bias-T, are included in figure B.1.

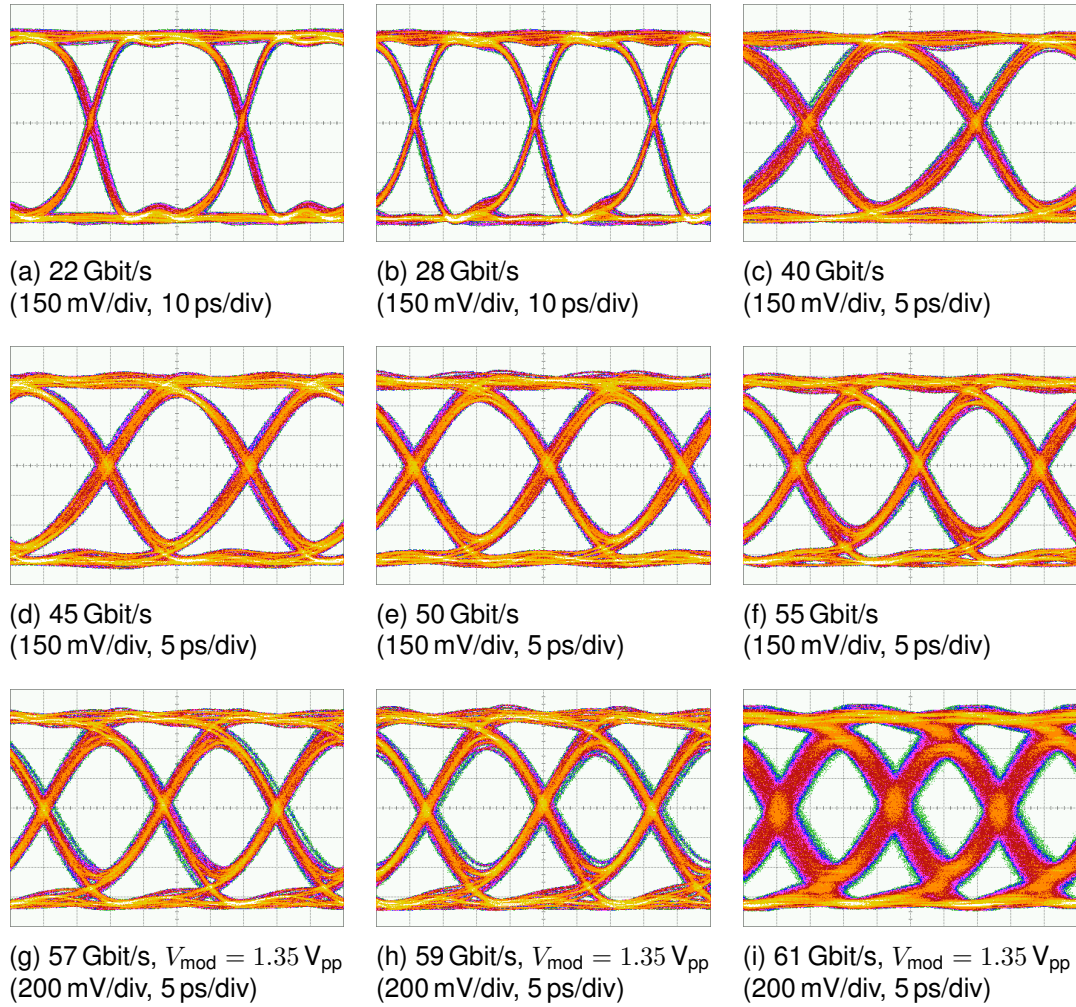


**Figure B.1:** Eye diagrams of the modulation signal obtained after the bias-T.  $V_{\text{mod}} = 0.99 V_{\text{pp}}$  if not stated otherwise.

## Appendix C

# Timing Jitter

In this appendix the additional jitter measurements have been plotted in figures C.1–C.5.

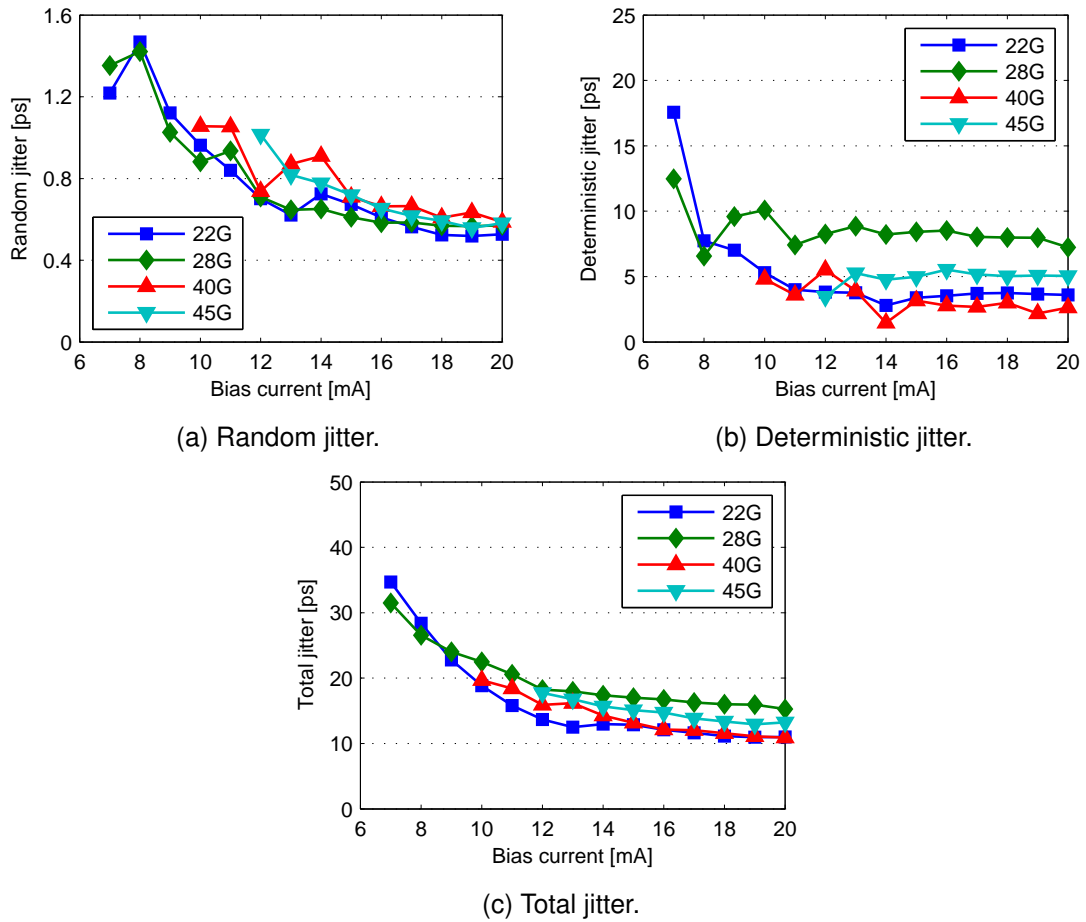
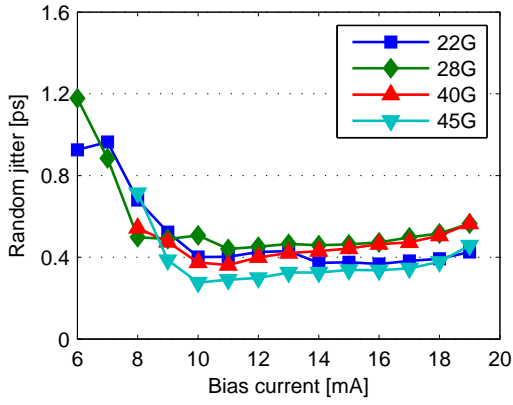
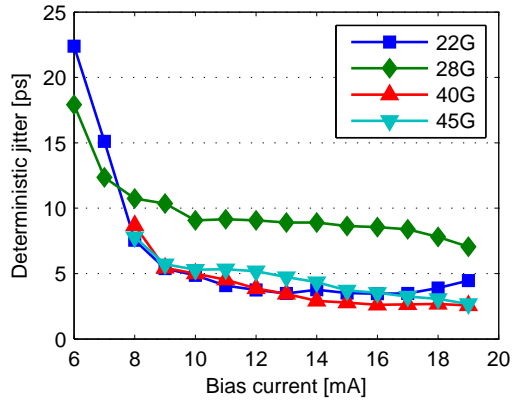


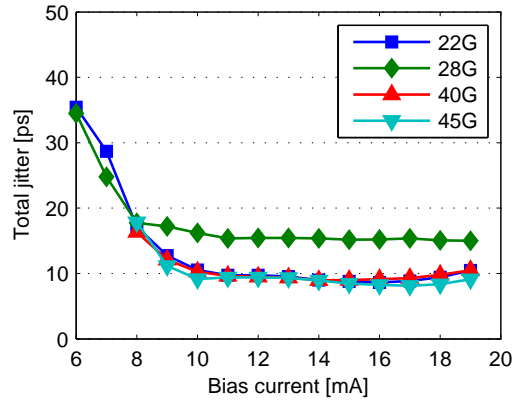
**Figure C.1:** Extracted values from jitter measurements BTB for VCSEL B using  $V_{\text{mod}} = 0.99 V_{\text{pp}}$ .



(a) Random jitter.



(b) Deterministic jitter.



(c) Total jitter.

**Figure C.2:** Extracted values from jitter measurements BTB for VCSEL C using  $V_{\text{mod}} = 0.99 V_{\text{pp}}$ .

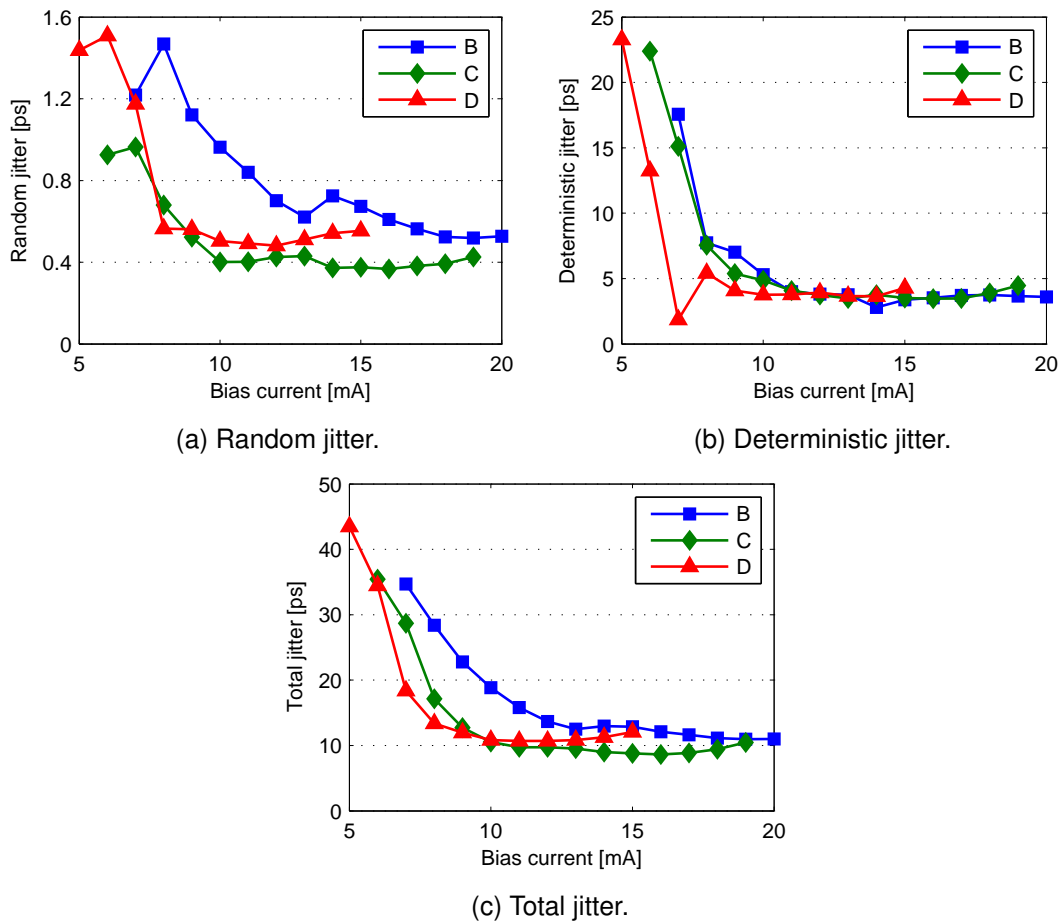
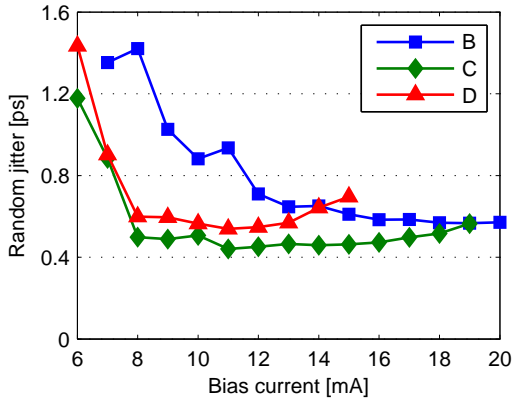
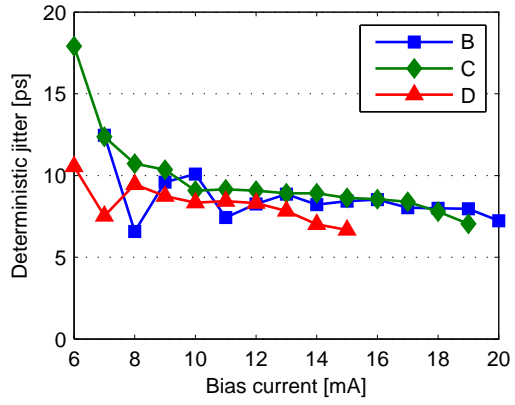


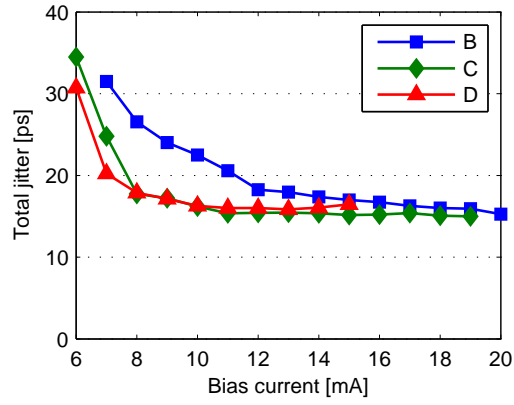
**Figure C.3:** Extracted values from jitter measurements BTB at 22 Gbit/s using  $V_{\text{mod}} = 0.99 V_{\text{pp}}$ .



(a) Random jitter.



(b) Deterministic jitter.



(c) Total jitter.

**Figure C.4:** Extracted values from jitter measurements BTB at 28 Gbit/s using  $V_{\text{mod}} = 0.99 V_{\text{pp}}$ .

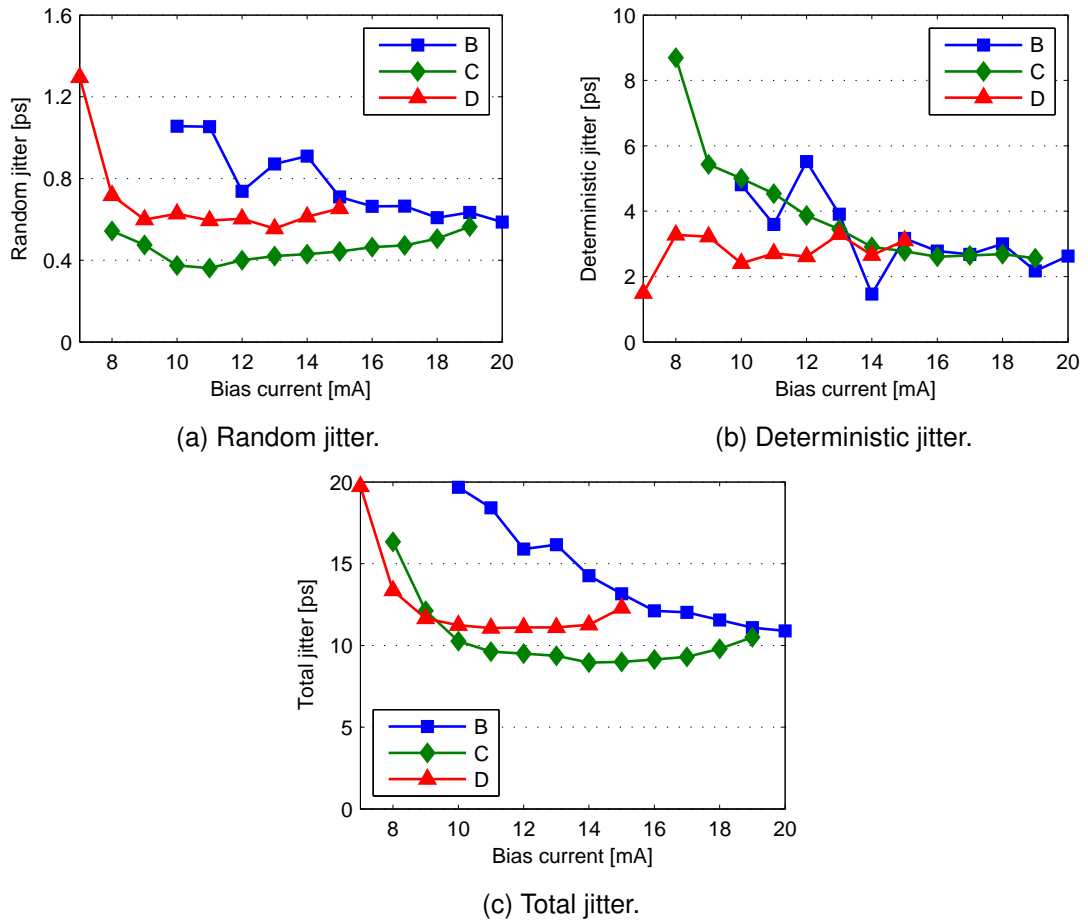


Figure C.5: Extracted values from jitter measurements BTB at 40 Gbit/s using  $V_{\text{mod}} = 0.99 V_{\text{pp}}$ .